

# Satellite Collision and Fragmentation Probabilities Using Radar-Based Size and Mass Estimates

Doyle T. Hall\* and Luis G. Baars†  
Omitron, Inc., Colorado Springs, Colorado 80903

<https://doi.org/10.2514/1.A35697>

Most conjunctions between Earth-orbiting satellites involve unknown objects, typically debris created by explosions or collisions. This study formulates methods to estimate probabilities of collision and fragmentation for such conjunctions, which depend on the estimated sizes and masses of the unknown objects. Analysis of radar cross-section (RCS) measurements provides estimated sizes, found to be accurate at the 90% confidence level to within a factor of 0.59 for potential underestimations and to within a factor of 3.1 for potential overestimations. For satellites that experience measurable atmospheric drag orbital perturbations, combining RCS data with orbit determination ballistic coefficients provides mass estimates accurate to within factors of 0.47 to 10.9 at the 90% confidence level. For satellites with perigee altitudes above 450 km, combining RCS data with solar radiation pressure coefficients provides mass estimates accurate to within factors of 0.44 to 5.6 at 90% confidence. The collision and fragmentation risk assessment formulation accounts for these size and mass estimation uncertainties. Specifically, conjunction collision probabilities formulated as statistically expected values account for the RCS-based size estimation uncertainties. Fragmentation probabilities, which measure the likelihood of producing more than a threshold number of collision fragments, account for both size and mass estimation uncertainties.

## Nomenclature

$A_j$	=	cross-sectional area projected by satellite	$\mathcal{L}_j$	=	length of $j$ th box-shaped calibration satellite
$\mathbf{a}$	=	vector of auxiliary variables required to calculate conjunction's collision probability	$M_j$	=	mass of $j$ th satellite
$B_j$	=	inverse ballistic coefficient of $j$ th satellite	$\mathcal{M}_j$	=	mass that characterizes atmospheric drag experienced by $j$ th satellite
$C_{D,j}$	=	aerodynamic drag coefficient of the $j$ th satellite	$M_{\max}$	=	maximum mass of primary and secondary objects
$C_{R,j}$	=	reflectivity coefficient of $j$ th satellite used for solar radiation pressure analysis	$M_{\min}$	=	minimum mass of primary and secondary objects
$D_j$	=	characteristic object size estimated for $j$ th satellite	$N_{\text{GH}}$	=	number of Gauss–Hermite quadrature coefficients
$D_{j,n}$	=	characteristic object size indicated by $n$ th radar cross-section measurement available for $j$ th satellite	$N_j^{\text{RCS}}$	=	number of radar cross-section measurements available for $j$ th satellite
$\mathbb{E}[-]$	=	expectation value operator, which indicates averaging over all relevant random variables	$N_s$	=	number of Monte Carlo samples ( $s$ spans the range $1 \dots N_s$ )
$F$	=	number of collisional fragments produced in collision between two satellites	$P_c$	=	collision probability for conjunction between two satellites
$F_{\text{EV}}(M_1, M_2)$	=	number of fragments produced by EVOLVE satellite collision model	$P_c(R)$	=	collision probability expressed as a function of the combined hard-body radius
$G_j$	=	inverse solar radiation pressure coefficient of $j$ th satellite	$\mathcal{P}_c(R, \mathbf{a})$	=	collision probability expressed as function of $R$ and vector of auxiliary variables, $\mathbf{a}$
$g_{\text{SEM}}(z)$	=	interpolation function for radar-cross-section-based characteristic size estimates	$\bar{P}_c$	=	statistically expected collision probability, in other words, equal to $\mathbb{E}[P_c(R)]$
$\mathcal{H}_j$	=	height of $j$ th box-shaped calibration satellite	$P_e$	=	effective HBR probability, approximated for conjunctions that satisfy small-hard-body-radius limit
$I_q(\bar{x}, \sigma_x)$	=	exponential expected value integral function; see Eq. (13)	$P_g$	=	steep-growth hard-body radius probability, approximated for conjunctions in steep-growth limit
$J$	=	number of known satellites used for hard-body radius or mass calibration analysis	$P_Q$	=	Monte Carlo probability quantile
$j$	=	index number of satellite	$Q$	=	quantile value for Monte Carlo probability estimates, $0 \leq Q \leq 1$
$L_c$	=	characteristic length of satellite, with $L_c \geq 0.05$ m used to approximate trackable objects	$R$	=	combined HBR for primary and secondary objects involved in conjunction, equal to $R_1 + R_2$
			$R_e$	=	effective HBR approximation, appropriate for conjunctions that satisfy small-hard-body-radius limit
			$R_g$	=	steep-growth HBR approximation, appropriate for conjunctions in steep-growth limit
			$R_j$	=	hard-body radius for $j$ th satellite
			$R_j^E$	=	known equivalent averaged projected area hard-body radius for $j$ th satellite
			$R_j^K$	=	known circumscribing hard-body radius for $j$ th satellite

Received 13 February 2023; revision received 0 ; accepted for publication 14 March 2023; published online Open Access 26 June 2023. Copyright © 2023 by the American Institute of Aeronautics and Astronautics, Inc. Under the copyright claimed herein, the U.S. Government has a royalty-free license to exercise all rights for Governmental purposes. All other rights are reserved by the copyright owner. All requests for copying and permission to reprint should be submitted to CCC at [www.copyright.com](http://www.copyright.com); employ the eISSN 1533-6794 to initiate your request. See also AIAA Rights and Permissions [www.aiaa.org/randp](http://www.aiaa.org/randp).

\*Senior Conjunction Assessment Research Scientist, 555 East Pikes Peak Avenue, #205.

†Conjunction Assessment Research Scientist, 555 East Pikes Peak Avenue, #205.

$s_Q$	=	sorted Monte Carlo sample number corresponding to quantile $Q$
$U(x)$	=	unit step function
$V_{\text{rel}}$	=	relative speed of conjunction between two satellites
$W_j$	=	combined inverse ballistic coefficient weights for $j$ th satellite
$W_{j,m}$	=	inverse ballistic coefficient weight for $m$ th VCM available for $j$ th satellite
$\mathcal{W}_j$	=	width of $j$ th box-shaped calibration satellite
$w_u$	=	$u$ th Gauss–Hermite quadrature coefficient
$x^K$	=	known value of quantity $x$ , denoted using superscript $K$
$x'_s$	=	$s$ th sample value for quantity $x$
$\bar{x}$	=	statistically expected (i.e., mean) value of quantity $x$ , in other words, equal to $\mathbb{E}[x]$
$Y_{j,n}$	=	radar cross-section in units of meters squared for $n$ th radar cross-section measurement available for $j$ th satellite
$z$	=	dimensionless radar cross-section value, equal to $Y_{j,n}/\lambda_{j,n}^2$
$z_s$	=	$s$ th sampled uniform random deviate
$\beta_{j,m}$	=	ballistic coefficient estimated in $m$ th vector covariance message available for $j$ th satellite
$\Delta\beta_{j,m}$	=	1-sigma uncertainty of ballistic coefficient estimated in $m$ th vector covariance message for $j$ th satellite
$\delta(x)$	=	unit impulse function (i.e., Dirac delta function)
$\mathcal{E}$	=	specific kinetic energy of collision between two satellites
$\mathcal{E}_*$	=	specific kinetic energy above which catastrophic collisions occur in EVOLVE model
$\Theta_j$	=	linear radar cross-section plus solar radiation pressure coefficient method mass calibration factor for $j$ th satellite
$\bar{\Theta}$	=	mean linear radar cross-section plus solar radiation pressure coefficient method mass calibration factor estimated from a set of cal. satellites
$\theta_j$	=	logarithmic radar cross-section plus solar radiation pressure coefficient method mass calibration factor for $j$ th satellite
$\bar{\theta}$	=	mean logarithmic radar cross-section plus solar radiation pressure coefficient mass calibration factor estimated from set of calibration satellites
$\lambda_{j,n}$	=	radar wavelength for $n$ th radar cross-section measurement available for $j$ th satellite
$\rho(x)$	=	probability density function of scalar quantity $x$
$\sigma_x^2$	=	variance of scalar quantity $x$ , in other words, equal to $\mathbb{E}[(x - \bar{x})^2]$
$\chi(x)$	=	cumulative distribution function of scalar quantity $x$
$\Psi_j$	=	linear radar cross-section plus ballistic coefficient method mass calibration factor for $j$ th satellite
$\bar{\Psi}$	=	mean linear radar cross-section plus ballistic coefficient method mass calibration factor estimated from set of cal. satellites
$\psi_j$	=	logarithmic radar cross-section plus ballistic coefficient method mass calibration factor for $j$ th satellite
$\bar{\psi}$	=	mean logarithmic radar cross-section plus ballistic coefficient method mass calibration factor estimated from set of cal. satellites
$\Omega_j$	=	linear hard-body radius calibration factor for $j$ th satellite
$\bar{\Omega}$	=	mean linear hard-body radius calibration factor estimated from set of calibration satellites
$\omega_j$	=	logarithmic hard-body radius calibration factor for $j$ th satellite
$\omega_{j,u}$	=	$u$ th Gauss–Hermite quadrature point for hard-body-radius calibration coefficient of $j$ th satellite

$\bar{\omega}$	=	mean logarithmic hard-body radius calibration factor estimated from set of calibration satellites
----------------	---	---

## I. Introduction

THE NASA Conjunction Assessment Risk Analysis (CARA) team assesses collision risks for a set of high-value Earth-orbiting satellites [1] based on the latest available satellite tracking data and orbit determination solutions [2]. For each conjunction, CARA initially assesses collision risk based on the probability of collision,  $P_c$ , which can be estimated using both semi-analytical [3–7] and Monte Carlo (MC) methods [8–10]. Many CARA high-value satellites reside in low Earth orbit (LEO), where most cataloged objects are tracked using ground-based radar systems, including the recently deployed Space Fence radar [11].

Conjunction collision probabilities depend on the sizes of the two satellites encountering one another as well as their relative trajectories and associated uncertainties [3–10]. This analysis focuses on the size-dependent aspect of  $P_c$  estimation. The size parameter often used for known satellites is the radius of the sphere circumscribing all of the fully deployed components of the spacecraft [5,12]. This *hard-body* radius (HBR) parameterization is both conservative (because it spans the full sphere circumscribing the satellite) and convenient (because it is a single, time-invariant parameter). The collision probability for a conjunction between a primary and secondary satellite that both have known sizes can be expressed as a function of the combined HBR,  $R = R_1 + R_2$ . Most conjunctions, however, represent encounters involving unknown objects, typically orbital debris created by on-orbit satellite explosions or collisions [13]. If available, radar cross-section measurements provide rough size estimates for such objects [14] and a means to approximate their unknown hard-body radii [15,16]. This study formulates collision probabilities as statistically expected values in order to account for uncertainties associated with the radar cross section based size estimation process.

Because a collision with any trackable object potentially could cause fatal damage to an active satellite, the collision probability represents a *mission protection* metric, focused on protecting the specific mission of a high-value satellite. Correspondingly, *environment protection* metrics focus on protecting Earth's orbital environment from the creation of large populations of collision fragmentation debris. The potential to produce such debris depends on the masses and relative velocity of the two objects [17]. This study formulates two environment protection metrics: the number of fragments statistically expected to be produced during a conjunction  $\bar{F}_c$  and the expected probability that an unacceptably large number of trackable fragments would be produced if a collision were to occur during a conjunction  $\bar{P}_F$ . Both depend on the sizes and masses of the primary and secondary satellites and their associated uncertainties.

As a first step, the analysis divides all tracked satellites into two fundamental types: known and unknown objects. Known objects have accurate tabulated HBR values and masses. The radar cross section based size analysis for unknown objects such as orbital debris aims to estimate HBR values along with associated uncertainties. Similarly, RCS- and orbit determination based mass analysis aims to estimate satellite masses and uncertainties. This study uses radar cross-section (RCS) measurements obtained by the Space Fence radar sensor, which provides data for about 90% of the LEO secondary objects involved in CARA conjunctions.

The majority of conjunctions that occur in Earth orbit involves two unknown objects. The potential for collisions to occur during such *unknown-on-unknown* conjunctions represents a long-term threat to Earth's orbital environment. This study formulates estimation methods to address all three generalized classes of conjunctions between tracked satellites: known-on-known (for which all sizes and masses are known), known-on-unknown (representing most of those currently processed by CARA), and unknown-on-unknown (for which all sizes and masses must be estimated from remote observations). For the latter two classes, the analysis focuses on RCS-based estimation methods, which apply to the majority of CARA conjunctions

because most of the secondary objects can be characterized using radar data. Many of the concepts used in the formulation, however, also apply to other remote sensing modalities (e.g., optical observations).

Section II of this paper summarizes previous work relevant to this study, including collision probability and fragmentation analysis methods, RCS-based size and mass estimation, and a description of current CARA risk assessment methods and archived conjunction data. Section III describes the new RCS-based size estimation formulation, including a description of the required calibration procedure and an analysis of the performance and accuracy of the method. Section IV similarly describes the RCS- and OD-based mass estimation formulation. Section V formulates methods to estimate collision probabilities that account for the RCS-based sizes and uncertainties, using both semi-analytical and Monte Carlo approaches. Section VI formulates Monte Carlo methods to assess collision fragmentation risks, which incorporate both the uncertain sizes and masses.

## II. Previous Work and Current Methods

This section briefly reviews previous work related to RCS-based collision and fragmentation risk assessments and summarizes the methods and data sets currently employed by CARA for conjunction processing.

### A. Conjunction Collision Probability Expressed as Function of Combined Hard-Body Radius

Many methods exist to estimate the collision probability for a conjunction between two tracked Earth-orbiting satellites, formulated using both semi-analytical approximations and MC techniques (e.g., Refs. [3–10]). Most express the probability of collision as a function of the combined HBR, in other words,  $P_c = P_c(R)$ , with  $R$  treated as a known and constant value, an approach that only strictly applies to the known-on-known class of conjunctions. Collision probabilities also depend on the orbital states and associated covariance matrices of the objects involved in the conjunction, but this formulation suppresses listing these parameters in the  $P_c$  function argument list for brevity.

In some formulations, conjunction collision probabilities also depend on other auxiliary variables which are often empirical in nature, such as process noise coefficients [18,19], dynamical consider parameters [20], covariance realism weights or scale factors [21,22], etc. These cases can be addressed by using an augmented collision probability function  $\mathcal{P}_c(R, \mathbf{a})$  with the vector  $\mathbf{a}$  representing the collected auxiliary variables. If  $\mathbf{a}$  has no uncertainty (or the uncertainty is neglected), then the augmented function itself provides an estimate for the collision probability, in other words,  $P_c(R) = \mathcal{P}_c(R, \mathbf{a})$ . The more realistic case in which  $\mathbf{a}$  has nonzero uncertainty requires a different approach. If a probability density function (PDF) that describes the uncertainty of the auxiliary variables is available, then the vector  $\mathbf{a}$  can be treated as a random variable [23], and a statistically expected value provides an estimate for collision probability:  $P_c(R) = \mathbb{E}[\mathcal{P}_c(R, \mathbf{a})]$ . (Note that in this study  $\mathbb{E}[\cdot]$  indicates the generalized statistical expectation value operator, which represents averaging over all applicable random variables [23], in other words, all of the elements of the vector  $\mathbf{a}$  in this case.) For instance, the dynamical consider parameter approach used by the Astrodynamics Support Workstation OD system (the space catalog system employed by the United States government) uses empirical global forecast atmospheric density auxiliary variables [20]. Preliminary analysis indicates that an uncertainty PDF for these empirical auxiliary variables can be estimated (which is a subject of ongoing CARA research), allowing the expected value method to be used in this case. In other cases, however, the elements of the vector  $\mathbf{a}$  might only be bounded using empirically determined upper and lower limits (as in the covariance scale factor method of Ref. [22], for instance). For these cases, a maximum-value analysis provides a conservative means to estimate the probability, in other words,  $P_c(R) = \max_{\mathbf{a}}[\mathcal{P}_c(R, \mathbf{a})]$ . If the vector  $\mathbf{a}$  represents a mixed set of random and bounded variables, then a hybrid approach to estimate  $P_c(R)$  is

required. As discussed later, estimating Monte Carlo quantiles and confidence intervals for collision and fragmentation probabilities depends on the uncertainties of these auxiliary variables, in addition to the uncertainties of the RCS-based sizes and masses.

This study uses the conjunction probability function  $P_c(R)$  as a starting point for the RCS-based formulation and assumes that uncertainties in auxiliary variables (if any exist) have already been accounted for using one of the methods described previously. In other words, this formulation treats the function  $P_c(R)$  as a *black box* and, other than assuming that it is a nondecreasing function of  $R$ , does not depend on the specific computational method used to estimate the  $P_c(R)$  probability function.

As mentioned previously,  $P_c(R) = P_c(R_1 + R_2)$  directly provides estimated collision probabilities for known-on-known conjunctions, which have known  $R_1$  and  $R_2$  values. Hejduk and Johnson [24] discuss  $P_c$ -based risk assessments for the known-on-unknown class of conjunctions, concluding that those analyses must account for RCS-based  $R_2$  estimation uncertainties. Similarly, the unknown-on-unknown class of conjunctions must account for uncertainties in both  $R_1$  and  $R_2$ .

### B. NASA RCS-Based Size Estimation Model

Stokely et al. [14] describe the NASA size estimation model (SEM), which provides a semi-empirical method to convert RCS measurements for an unknown satellite into a statistical ensemble of estimates for the *characteristic length* of the object. This characteristic length is not equivalent to the hard-body radius but instead represents the average of the largest dimensions of an object measured along three orthogonal axes [14], which corresponds to the diameter for spherical objects. Applying the SEM to the  $n$ th RCS measurement available for the  $j$ th satellite yields

$$D_{j,n} = \begin{cases} \lambda_{j,n} \sqrt{4z/\pi} & z > 5 \\ \lambda_{j,n} \left[ \sqrt[6]{4z/(9\pi^5)} \right] & z < 0.03 \\ \lambda_{j,n} g_{\text{SEM}}(z) & \text{otherwise} \end{cases} \quad (1)$$

with  $D_{j,n}$  denoting the characteristic length (meters) corresponding to the RCS measurement,  $\lambda_{j,n}$  denoting the radar wavelength (meters), and  $z = Y_{j,n}/\lambda_{j,n}^2$ , with  $Y_{j,n}$  representing the measured RCS value (meters squared). Stokely et al. [14] provide an interpolation table for the function  $g_{\text{SEM}}(z)$ . Notably, the NASA SEM provides no direct means to estimate the error or uncertainty of RCS-based characteristic length estimates. This can be especially problematic if only one representative (e.g., median) RCS value is available per satellite. As described later, this study uses data sets comprising numerous RCS measurements per satellite observed over extended time periods (e.g., approximately 1000 RCS measurements acquired over approximately two years) and analyzes the resulting characteristic length distributions in order to estimate both the unknown hard-body radii and associated uncertainties.

### C. NASA EVOLVE Collision Fragmentation Model

Johnson et al. [17] describe an empirical method of roughly approximating the number of fragments produced by an on-orbit collision, based on laboratory studies of high-velocity impacts, as developed for the NASA EVOLVE orbital debris model. The approximation requires as input the masses of the two objects  $M_1$  and  $M_2$  as well as the magnitude of their relative velocity  $V_{\text{rel}}$ . The number of fragments depends on whether the conjunction could result in a *catastrophic* collision that causes nearly complete fragmentation of both objects or a *noncatastrophic* collision, which causes significantly less fragmentation (e.g., by the lighter object only creating a crater on the heavier object's surface or an isolated puncture through one of its solar panels). The catastrophic vs noncatastrophic determination uses the specific kinetic energy of the event [17]

$$\mathcal{E}(M_1, M_2) = \frac{M_{\min}}{M_{\max}} \left( \frac{V_{\text{rel}}^2}{2} \right) \quad (2)$$

with  $M_{\min} = \min(M_1, M_2)$  and  $M_{\max} = \max(M_1, M_2)$ . Catastrophic collisions occur in the model if  $\mathcal{E}(M_1, M_2)$  exceeds a threshold of  $\mathcal{E}_* = 40,000$  J/kg. Because  $M_{\min}/M_{\max}$  is less than or equal to 1 by definition, catastrophic collisions potentially occur in the model only for sufficiently high relative speeds, specifically  $V_{\text{rel}} > \sqrt{2\mathcal{E}_*} \approx 0.3$  km/s. Figure 1 shows a histogram of  $V_{\text{rel}}$  for approximately 400 k conjunctions recorded in CARA's archive over a recent two-year period, indicating that most had relative speeds capable of producing catastrophic collisions. For a given  $V_{\text{rel}}$  value, a catastrophic collision occurs in the EVOLVE model for  $M_{\min}/M_{\max} > 2\mathcal{E}_*/V_{\text{rel}}^2$ . This means that, for a typical CARA conjunction with  $V_{\text{rel}} \approx 15$  km/s, a secondary object with only about 0.04% the mass of the primary satellite has the potential to create a catastrophic collision in the EVOLVE model. For a smaller relative speed of  $V_{\text{rel}} \approx 1$  km/s, however, a secondary with mass  $\geq 8\%$  of that of the primary is required for a catastrophic collision in the model.

The number of fragments produced in the EVOLVE model differs greatly for catastrophic and noncatastrophic collisions and empirically depends on the object masses as [17]

$$F_{\text{EV}}(M_1, M_2) = \begin{cases} 0.1 \left( \frac{V_{\text{rel}} M_{\min}}{V_0 M_0} \right)^{0.75} \left( \frac{L_c}{L_0} \right)^{-1.71} & \text{if } \mathcal{E} \leq \mathcal{E}_* \text{ (noncatastrophic)} \\ 0.1 \left( \frac{M_1 + M_2}{M_0} \right)^{0.75} \left( \frac{L_c}{L_0} \right)^{-1.71} & \text{if } \mathcal{E} > \mathcal{E}_* \text{ (catastrophic)} \end{cases} \quad (3)$$

with  $V_0 = 1$  km/s,  $M_0 = 1$  kg, and  $L_0 = 1$  m. As in previous analyses [15,16], this study approximates *trackable* fragments as those with characteristic lengths exceeding a cutoff of  $L_c = 0.05$  m. For known-on-known conjunctions, Eq. (3) directly estimates the number of fragments. For known-on-unknown conjunctions, however, calculating the expected number of fragments requires accounting for the uncertainty of the estimated secondary mass,  $M_2$ . For unknown-on-unknown conjunctions, the calculation must account for uncertainties in both  $M_1$  and  $M_2$ .

## D. Unknown Object Mass Estimation

Lechtenberg [16] formulates an RCS- and OD-based method to estimate masses of LEO satellites in order to assess fragmentation risks, concluding that such mass estimates can be highly uncertain and recommending a conservative uncertainty confidence level (e.g., the 99.9th percentile) when choosing a single representative mass for

conjunction risk assessments. This study aims to extend that formulation, but using a different methodology that eliminates the need to choose a single mass based on a conservative (but otherwise arbitrary) confidence level. More specifically, this formulation empirically calibrates the mass estimation process and quantifies the associated uncertainties, in order to estimate risk assessment metrics as statistical expectation values.

Combining RCS-based projected area estimates with OD-based ballistic coefficient estimates provides one means to approximate the masses of LEO object masses [15,16]. Ballistic coefficients describe the atmospheric drag force exerted on satellites that have altitudes low enough to experience measurable orbital decay [25]. The relationship for a satellite that experiences measurable atmospheric drag orbital perturbations is  $M = ABC_D$ , with  $M$  indicating the mass of the satellite,  $A$  indicating the cross-sectional area it projects in the direction perpendicular to the relative atmospheric flow,  $B = 1/\beta$  indicating the inverse ballistic coefficient, and  $C_D$  indicating the drag coefficient [15,16,25].

In addition to estimating *RCS+BC* mass values that combine RCS-based projected area estimates with OD-based ballistic coefficient estimates, this analysis also estimates *RCS+SRPC* mass values, by similarly combining RCS-based area estimates with OD-based solar radiation pressure coefficient estimates. The relationship for a satellite that experiences measurable solar radiation pressure (SRP) perturbations is  $M = AGC_R$ , with  $A$  indicating in this case the cross-sectional area projected toward the incident sunlight,  $G$  indicating the inverse SRP coefficient, and  $C_R$  indicating the reflectivity coefficient [25]. As discussed later, both of these methods provide rough mass estimates, although comparison with a set of objects with known masses indicates that, for satellites above 450 km altitude, SRP mass estimates are somewhat more accurate.

## E. Current and Future CARA Estimation Methods

The CARA system processes mostly known-on-unknown conjunctions, along with some known-on-known conjunctions. The system currently approximates known-on-unknown conjunctions using a fixed secondary HBR of  $R_2 = 1.5$  m, which tends to overestimate  $P_c$  values, as discussed later. A more accurate approach entails using  $R_2$  estimates specifically determined for each secondary satellite involved in each conjunction. This study focuses on developing RCS-based HBR estimation methods for the unknown objects. A parallel CARA effort focuses on tabulating HBR values for known satellites, including active and retired payloads as well as rocket bodies and operational debris (e.g., fairings, shrouds, lens caps, etc.). Together, these efforts constitute CARA's *dynamic HBR* analysis task, which aims to improve risk assessment methods for the protection of high-value satellite missions.

Currently, CARA does not operationally use any metrics to assess fragment production risks to the orbital environment, although the subject has been researched [15,16,26]. Collision fragment populations depend sensitively on the masses of the two objects encountering one another [17]. This study focuses on RCS- and OD-based mass estimation methods for unknown objects, and a parallel CARA effort focuses on tabulating the masses of known satellites. Together, these efforts constitute CARA's *collision consequence* analysis task, which aims to develop risk assessment methods for the protection of Earth's orbital environment.

## F. Archived CARA Conjunction Data

This analysis applies the newly developed risk assessment methods to a set of 410,674 conjunctions, archived in the CARA database during the ten-month period 1 September 2020 to 30 June 2021. The database contains the close approach orbital states and covariance matrices required to calculate collision probabilities for each conjunction; in most cases, it also contains the dynamic consider parameter data required to apply covariance correlation corrections as described by Casali et al. [20]. The archived conjunctions involve 67 unique primary objects with known HBR values spanning the range  $2.5 \leq R_1^K \leq 26$  m (the superscript  $K$  indicates known quantities), with a median of 7 m. The primary masses span the range

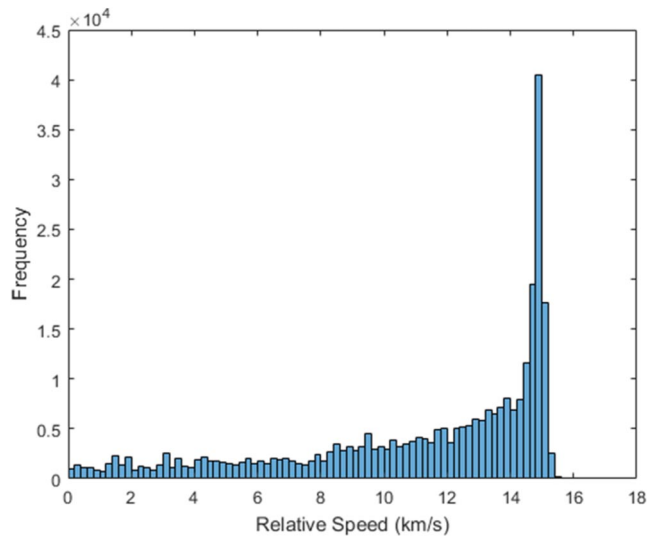


Fig. 1 The relative speed for approximately 400k CARA conjunctions.

$18 \leq M_1^K \leq 12,000$  kg, with a median of 1200 kg. Among the 410,674 analyzed conjunctions, 147,404 (36%) involve secondary objects that have known HBRs and masses. Among these, 33,371 also involve relatively small secondary objects with  $R_2^K \leq 0.35$  m, which have sufficient auxiliary RCS and ballistic coefficient data to allow size and mass estimation, a subset used to evaluate the performance of the newly formulated methods. Among the 410,674 analyzed conjunctions 247,049 (60.2%) involve secondary objects with unknown HBRs and masses. Of these 247,049 known-on-unknown conjunctions, 225,695 (91%) have sufficient auxiliary data to allow secondary object size and mass estimation.

### III. Estimating Sizes of Unknown Objects

Calculating collision probabilities for conjunctions involving unknown objects requires estimating the unknown hard-body radii. This section develops a method of analyzing a set of known satellites in order to calibrate the RCS-based HBR estimation process and quantify the associated uncertainties. The specific results presented in this section employ Space Fence RCS data collected within the two years before the calibration epoch date of 15 January 2022. The analysis is restricted to objects with 20 or more well calibrated and quality-curated Space Fence system RCS measurements, as described in detail by Baars and Hall [27]. Typical CARA secondary objects have between 200 and 1500 such RCS measurements.

#### A. Estimating RCS-Based Characteristic Lengths of Unknown Objects

As a first step toward estimating unknown HBR values and uncertainty distributions, this analysis uses the NASA size estimation model to estimate RCS-based characteristic sizes. Applying Eq. (1) to the  $j$ th satellite produces a set of characteristic length estimates,  $\{D_{j,n}, n = 1 \dots N_j^{\text{RCS}}\}$ , which typically has considerable point-to-point variability or scatter. Sources of this scatter include the object's aspect-dependent radar reflection properties and projected area (which vary in time due to rotation and changing observational geometry) as well as RCS measurement noise (which is often relatively minor). The formulation approximates satellite characteristic length uncertainties using an empirical cumulative distribution function (CDF) which includes the entire set of available RCS-based estimates, as follows:

$$\chi(D_j) = \frac{1}{N_j^{\text{RCS}}} \sum_{n=1}^{N_j^{\text{RCS}}} U(D_j - D_{j,n}) \quad \text{with} \quad U(x) = \begin{cases} 0 & x \leq 0 \\ 1 & x > 0 \end{cases} \quad (4)$$

The corresponding empirical PDF is

$$\rho(D_j) = \frac{1}{N_j^{\text{RCS}}} \sum_{n=1}^{N_j^{\text{RCS}}} \delta(D_j - D_{j,n}) \quad \text{with} \quad \delta(x) = \frac{dU(x)}{dx} \quad (5)$$

In these equations,  $U(x)$  denotes the unit step function, and  $\delta(x)$  denotes the unit impulse function, in other words, the Dirac delta function [28]. [Note that this study uses the symbols  $\chi$  and  $\rho$  for generalized CDF and PDF representations, respectively, such that  $\rho(x)$  represents the PDF of the random variable  $x$ ,  $\chi(y)$  represents the CDF of random variable  $y$ , etc.]

Using the empirical PDF approximation, the statistically expected (or mean) characteristic length for the  $j$ th satellite is

$$\bar{D}_j = \mathbb{E}[D_j] = \int_0^\infty \rho(D_j)[D_j] dD_j \approx \frac{1}{N_j^{\text{RCS}}} \sum_{n=1}^{N_j^{\text{RCS}}} D_{j,n} \quad (6)$$

The corresponding variance is

$$\sigma_{D_j}^2 = \mathbb{E}[(D_j - \bar{D}_j)^2] \approx \frac{1}{N_j^{\text{RCS}}} \sum_{n=1}^{N_j^{\text{RCS}}} (D_{j,n} - \bar{D}_j)^2 \quad (7)$$

Because the variable radar reflection properties of a satellite causes some of the variation of the  $D_{j,n}$  values, the empirical PDF approximation tends to overestimate the variance of the object's actual characteristic size distribution.

#### B. Calibrating the Hard-Body Radius Estimation Process

If the SEM were free of any estimation inaccuracies and the RCS measurements were free of any measurement noise, then the relationship between the circumscribing HBR and the characteristic length for idealized spherical objects would be relatively simple:  $R_j = D_j/2$ . To quantify the bias and uncertainty for noisy measurements of actual nonspherical objects, this analysis introduces a calibration factor into this relationship, expressed in either linear or logarithmic form as follows:

$$R_j = \Omega_j(D_j/2) = e^{\omega_j}(D_j/2) \quad (8)$$

The formulation assumes that the calibration factors  $\Omega_j$  and  $\omega_j = \log_e(\Omega_j) = \ln(\Omega_j)$  are time invariant but that they vary from satellite to satellite. As described in the following, analysis of RCS data for a large set of known satellites provides the means to estimate the average logarithmic calibration factor and its uncertainty. The method assumes that the known calibration satellites have size and radar reflection properties comparable to those of typical unknown satellites.

As in previous size analyses [15,16], this study uses a set of relatively small calibration satellites that all have convex cuboid shapes. Specifically, the calibration analysis employs sizes obtained from the *Database and Information System Characterizing Objects in Space* (DISCOS), which tabulates the bounding dimensions and general shape descriptions of a large number of known satellites [29,30]. The calibration analysis is restricted to satellites labeled as *box* shaped in the DISCOS database and that have no tabulated additional panels or attachments. The circumscribing HBR for a box-shaped satellite with sides of length  $\mathcal{L}_j$ , width  $\mathcal{W}_j$ , and height  $\mathcal{H}_j$  is given by

$$R_j^K = \frac{1}{2} \sqrt{\mathcal{L}_j^2 + \mathcal{W}_j^2 + \mathcal{H}_j^2} \quad (9)$$

The calibration analysis is also restricted to DISCOS satellites with  $R_j^K \leq 0.35$  m, which are comparably small to the typical unknown debris objects involved in CARA conjunctions (as discussed in more detail later).

Space Fence observations collected in the two years preceding the calibration epoch date of 15 January 2022 provide usable RCS measurements for 586 of the box-shaped satellites tabulated in the DISCOS database. Each of these provides an independent (albeit noisy) measurement of the logarithmic calibration factor

$$\omega_j = \ln(2R_j^K/\bar{D}_j) \quad (10)$$

Analysis indicates that the observed distribution of the logarithmic  $\omega_j$  factors matches a Gaussian distribution significantly better than that of the linear  $\Omega_j$  factors. Sivia and Skilling [31] present a Bayesian analysis approach that can be used to estimate the mean logarithmic calibration factor from the set  $\{\omega_j, j = 1 \dots J\}$ , with  $J = 586$ , in this case. The method assumes that satellite-to-satellite variations in the  $\omega_j$  values are Gaussian distributed and applies an uninformed-prior Bayesian analysis method to derive the maximum posterior estimates for the mean calibration factor and variance [31]

$$\bar{\omega} = \frac{1}{J} \sum_{j=1}^J \omega_j \quad \text{and} \quad \sigma_\omega^2 = \frac{1}{J-1} \sum_{j=1}^J [\omega_j - \bar{\omega}]^2 \quad (11)$$

For the 15 January 2022 calibration data, the analysis yields  $\bar{\omega} = 0.319$  and  $\sigma_\omega = 0.507$ . The estimate for  $\sigma_\omega$  indicates significant satellite-to-satellite variation in the calibration factors, approximated using a PDF in the form of a Gaussian (i.e., normal) distribution



$$\rho(\omega) \approx \mathcal{N}(\omega, \bar{\omega}, \sigma_\omega^2) = (2\pi\sigma_\omega^2)^{-1/2} \exp\left[-\frac{(\omega - \bar{\omega})^2}{2\sigma_\omega^2}\right] \quad (12)$$

Using this PDF, the linear mean calibration factor is estimated to be  $\bar{\Omega} = \mathbb{E}[e^\omega] = I_1(\bar{\omega}, \sigma_\omega) = 1.56$ , which is calculated using the exponential expected value integral function given by

$$I_q(\bar{\omega}, \sigma_\omega) = \mathbb{E}[e^{q\omega}] = e^{q\bar{\omega} + q^2\sigma_\omega^2/2} \quad (13)$$

with  $q = 1$ , in this case.

To assess the accuracy of the calibrated estimation process, Fig. 2 compares the CDF of the ratio of statistically expected calibrated HBR values  $\bar{R}_j$  to the known values  $R_j^K$  for the 586 satellites. (The next section describes how  $\bar{R}_j$  values are calculated.) The CDF indicates that, among this population, calibration uncertainties limit the 90% confidence accuracy range of the HBR estimation process to within a factor of 0.59 for potential underestimations and to within a factor of 3.1 for potential overestimations.

### C. Estimating Statistically Expected Hard-Body Radii

The statistically expected HBR of the  $j$ th satellite accounts for uncertainties in both the characteristic size estimation and the HBR calibration process, as expressed by a double integral

$$\bar{R}_j = \mathbb{E}[e^{\omega_j}(D_j/2)] = \int_0^\infty \rho(D_j) \left\{ \int_{-\infty}^\infty \rho(\omega) [e^\omega (D_j/2)] d\omega \right\} dD_j \quad (14)$$

Using the PDF approximations given in Eqs. (5) and (12) allows analytical evaluation of both integrals, yielding

$$\bar{R}_j \approx \frac{\bar{D}_j I_1(\bar{\omega}, \sigma_\omega)}{2} \quad (15)$$

with  $\bar{D}_j$  given by Eq. (6) and  $I_1(\bar{\omega}, \sigma_\omega)$  given by Eq. (13). The associated variance also has an analytical approximation

$$\sigma_{\bar{R}_j}^2 \approx \left[ \frac{(\bar{D}_j^2 + \sigma_{D_j}^2) I_2(\bar{\omega}, \sigma_\omega)}{4} \right] - \bar{R}_j^2 \quad (16)$$

with  $\sigma_{D_j}^2$  given by Eq. (7). As mentioned previously in Sec. V.A, using the empirical PDF of Eq. (5) tends to result in overestimated  $\sigma_{D_j}^2$  values, which in turn leads to both  $\bar{R}_j$  and  $\sigma_{\bar{R}_j}^2$  being overestimated.

Analysis of the 225,695 known-on-unknown conjunctions that have sufficient RCS data to allow size and mass estimation indicates that most unknown secondary objects have small estimated sizes relative to the primary satellites. Specifically, 97.7% of the conjunctions involve secondary objects with  $\bar{R}_2 \leq 0.35$  m. This means that

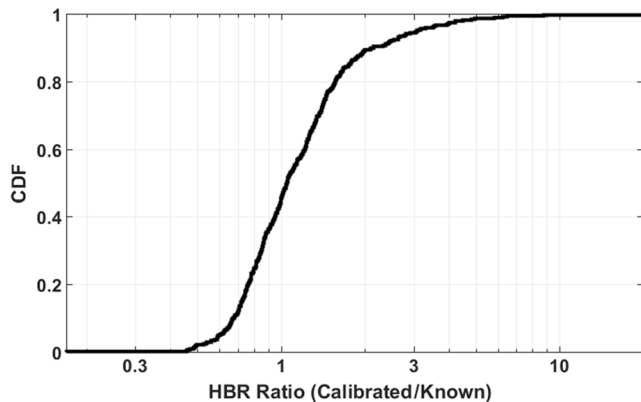


Fig. 2 CDF of the ratio of calibrated HBR values to known HBR values for 586 cuboid satellites.

typical secondary objects are much smaller than the median CARA primary, with an HBR of 7 m. This predominance of relatively small objects is the reason that the HBR calibration analysis presented in the previous section was restricted to DISCOS satellites with  $R_j^K \leq 0.35$  m. In addition, only 0.3% of the known-on-unknown conjunctions have  $\bar{R}_2 > 1.5$  m. This means that the default HBR value of 1.5 m currently used by the CARA processing system tends to overestimate the size of unknown secondary objects, which leads to overestimated  $P_c$  values as shown in more quantitative detail later.

### D. Estimating Equivalent Projected Area Hard-Body Radii

As mentioned earlier, the circumscribing HBR provides a conservative and convenient parameterization of a satellite's size for collision probability estimation. However, as discussed by Mashiku and Hejduk [12], the *equivalent area* HBR (which corresponds to a satellite's projected area realized as a circle) provides an alternate, less conservative parameterization. Cauchy's projected area theorem [32] indicates that the aspect-averaged projected area for any convex object equals 25% of the total surface area, which implies that the equivalent area HBR for a box-shaped satellite is

$$R_j^E = \sqrt{\frac{\mathcal{L}_j \mathcal{W}_j + \mathcal{L}_j \mathcal{H}_j + \mathcal{W}_j \mathcal{H}_j}{2\pi}} \quad (17)$$

Repeating the HBR calibration process using  $R_j^E$  values instead of the known circumscribing HBR values  $R_j^K$  given by Eq. (9) yields  $\bar{\omega} = 3.48 \times 10^{-4}$  and  $\sigma_\omega = 0.502$ , for the 15 January 2022 calibration data. Notably, the  $\sigma_\omega$  values calculated for the circumscribing and equivalent area HBR methods are relatively similar, 0.526 vs 0.502, meaning that both provide HBR estimates of comparable uncertainty. However, the mean linear calibration factor for equivalent area HBR estimation,  $\bar{\Omega} = 1.14$ , is 27% smaller than that for circumscribing HBR estimation,  $\bar{\Omega} = 1.56$ . This means that, for unknown objects, calibrated equivalent area HBR values will be about three-quarters as large as calibrated circumscribing HBR values, systematically. This study uses the more conservative circumscribing HBR method to estimate collision and fragmentation probabilities for unknown objects, but the analysis produces qualitatively similar results using either method.

### E. Performance of RCS-Based Hard-Body Radius Estimation

As mentioned previously, among the 410,674 CARA conjunctions analyzed in this study, a total of 33,371 involve known secondary objects that have relatively small HBR values (i.e.,  $R_2^K \leq 0.35$  m) and that also have sufficient RCS data to allow HBR estimation. This set of *small-secondary* conjunctions provides a means of testing how well the RCS-based estimation method performs for objects that are small enough to represent reasonable surrogates for the truly unknown secondary population. Figure 3 compares the combined

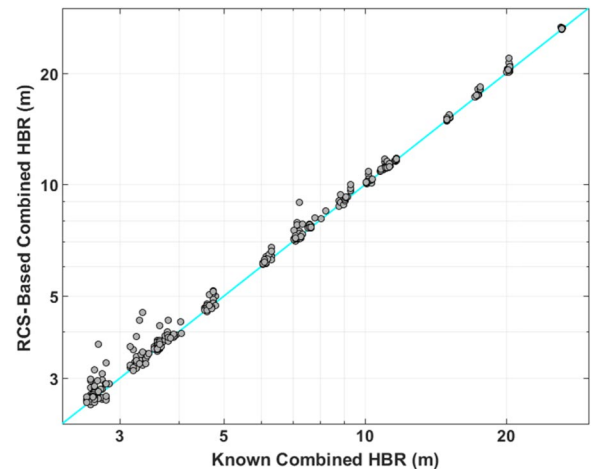


Fig. 3 Hard-body radii for conjunctions involving small secondary objects.

hard-body radii for these conjunctions by plotting  $R_1^K + \bar{R}_2$  vs  $R_1^K + R_2^K$ . Many of the RCS-based combined HBR estimates match the known estimates reasonably accurately. In addition, for the most of the discrepant cases, the RCS-based values tend to overestimate the known values, as discussed in Sec. III.A, which in turn will lead to conservatively large collision probability estimates.

#### IV. Estimating Masses of Unknown Satellites

The process of calibrating and estimating LEO satellite masses is similar to that described previously for HBR values, but somewhat more complicated because it combines RCS-based projected area estimates with OD-based ballistic coefficient (BC) or solar radiation pressure coefficient (SRPC) estimates. Unfortunately, accounting for the uncertainties in these additional parameters requires several approximations, which results in final mass estimates that have significant (but quantifiable) uncertainties. The results presented in this section combine the Space Fence RCS data collected within the two years before the calibration epoch of 15 January 2022, with OD-based BC or SRPC values estimated within the six months before that date. Specifically, the analysis uses a series of OD state and covariance solutions as supplied in Vector Covariance Messages (VCMs), each separated by one week or more in time. (The VCM format used by the United States government reports a satellite's precision state and covariance at an OD epoch time, accompanied by metadata giving details about the fit to the tracking data.) The analysis imposes a VCM separation of one week or more in an effort to obtain a series of statistically independent OD solutions, or at least nearly independent solutions [27].

##### A. Estimating RCS- and BC-Based Mass for Satellites Experiencing Atmospheric Drag Perturbations

Combining RCS-based size estimates and OD-based BC estimates provides a means to estimate the masses of satellites that experience measureable atmospheric drag. This *RCS+BC* mass estimation method approximates the characteristic mass of a satellite using an expression formulated previously [16],

$$\mathcal{M}_{D,j} = A_j B_j C_{D,j} \approx (\pi D_j^2/4) B_j C_{D,j} \quad (18)$$

In this expression,  $\mathcal{M}_{D,j}$  indicates the mass that characterizes the atmospheric drag experienced by the  $j$ th satellite, which is proportional to the product of the projected area  $A_j$ , the inverse ballistic coefficient  $B_j$ , and the drag coefficient  $C_{D,j}$  (also see Refs. [15,25]). The analysis uses RCS-based characteristic projected areas to estimate satellite cross sectional areas projected normal to the local atmospheric flow,  $A_j \approx (\pi D_j^2/4)$ , which is a rough approximation, especially for highly elongated or flattened objects. As before, this study introduces a positive scalar calibration factor  $\Psi_j$  into Eq. (18) to quantify the bias and uncertainty of the RCS+BC mass estimation process

$$M_j \approx \Psi_j \mathcal{M}_{D,j} = e^{\psi_j} [(\pi D_j^2/4) B_j C_{D,j}] \quad (19)$$

with  $M_j$  indicating the calibrated mass of the satellite,  $\Psi_j$  indicating the linear calibration factor, and  $\psi_j$  indicating the logarithmic calibration factor. As before, the analysis assumes the calibration factors are time invariant but vary from satellite to satellite. Also as before, analysis indicates that the distribution of the logarithmic  $\psi_j$  factors matches a Gaussian distribution significantly better than that of the linear  $\Psi_j$  factors. Applying Eq. (19) to the  $j$ th calibration satellite yields

$$M_j^K = e^{\psi_j} \mathbb{E}[\mathcal{M}_j] \approx e^{\psi_j} [\bar{A}_j \bar{B}_j \bar{C}_{D,j}] \quad (20)$$

As in previous analyses [15,16], this approximation neglects correlations between the quantities  $D_j$ ,  $B_j$ , and  $C_{D,j}$ . Also, the projected area is approximated using the empirical PDF given by Eq. (5),

yielding a statistically expected value of  $\bar{A}_j = \mathbb{E}[A_j] \approx \pi(\bar{D}_j^2 + \sigma_{D_j}^2)/4$ .

The formulation approximates the inverse ballistic coefficient PDF, by first empirically estimating the ballistic coefficient mean and variance parameters and then assuming a lognormal distribution of the form

$$\rho(B_j) \approx \frac{\mathcal{N}(\ln(B_j), \bar{b}_j, \sigma_{b_j}^2)}{B_j} \quad (21)$$

with  $\sigma_{b_j}^2 = \ln(1 + \sigma_{B_j}^2/\bar{B}_j^2)$  and  $\bar{b}_j = \ln(\bar{B}_j) - \sigma_{b_j}^2/2$ . (Note that sampling this PDF, as will later be required for Monte Carlo estimations, cannot produce negative  $B_j$  values, which are physically unrealistic for satellites that experience measureable levels of atmospheric drag. This is why this analysis does not assume a PDF of the form  $\mathcal{N}(B_j, \bar{B}_j, \sigma_{B_j}^2)$ , which can potentially produce negative sampled values.) The mean and variance of the inverse ballistic coefficient,  $\bar{B}_j$  and  $\sigma_{B_j}^2$ , respectively, are estimated empirically by combining a series of OD solutions accumulated over the six months before the calibration epoch date. Specifically, the analysis uses a series of VCMs separated by one week or more in time that each represent an OD solution for the  $j$ th satellite. The corresponding ballistic coefficients,  $\{\beta_{j,m}, \Delta\beta_{j,m}\}, m = 1 \dots N_j^{\text{VCM}}\}$ , typically number  $N_j^{\text{VCM}} \approx 25$  for most satellites. (This study considers atmospheric drag effects not to be *measurable* if none of the available VCMs provides a usable, positive-valued ballistic coefficient, which can occur for high-altitude satellites.) The ballistic coefficients  $\beta_{j,m}$  and associated 1-sigma OD estimation uncertainties  $\Delta\beta_{j,m}$  are then combined using a weighted averaging scheme. The first step in the process is to calculate the inverse ballistic coefficient and uncertainty for the  $m$ th VCM available for the  $j$ th satellite

$$B_{j,m} = 1/\beta_{j,m} \text{ and } \Delta B_{j,m} = \Delta\beta_{j,m}/\beta_{j,m}^2 \quad (22)$$

The next step calculates the weighted average

$$\bar{B}_j = \frac{1}{W_j} \sum_{m=1}^{N_j^{\text{VCM}}} W_{j,m} B_{j,m} \quad (23)$$

with  $W_{j,m} = (\Delta B_{j,m})^{-2}$  and  $W_j = \sum_m W_{j,m}$ . The analysis estimates the variance using a hybrid scheme as

$$\sigma_{B_j}^2 = \max(W_j^{-1}, V_j) \quad (24)$$

with

$$V_j = W_j^{-1} \left[ \frac{N_j^{\text{VCM}}}{N_j^{\text{VCM}} - 1} \sum_{m=1}^{N_j^{\text{VCM}}} W_{j,m} (B_{j,m} - \bar{B}_j)^2 \right]^{1/2} \quad (25)$$

This scheme conservatively uses the larger of the variances estimated using two methods: the first assumes statistical independence of the  $B_{j,m}$  values, yielding variance equal to  $W_j^{-1}$ , and the second accounts for the observed scatter of the  $B_{j,m}$  values, yielding the empirically estimated variance equal to  $V_j$  [33]. In the rare cases when only one OD solution is available for an object (i.e.,  $N_j^{\text{VCM}} = 1$ ), the analysis uses  $\sigma_{B_j}^2 = W_j^{-1} = (\Delta B_{j,m})^2$  for the variance.

Finally, the analysis approximates the PDF for the satellite drag coefficients  $C_{D,j}$  using a uniform distribution spanning a fixed, bounded range

$$\rho(C_{D,j}) \approx \begin{cases} (C_{D,\max} - C_{D,\min})^{-1} & \text{if } C_{D,\min} \leq C_{D,j} \leq C_{D,\max} \\ 0 & \text{otherwise} \end{cases} \quad (26)$$

This study uses the bounds  $C_{D,\min} = 2.1$  and  $C_{D,\max} = 2.9$  for all objects, based on the range of drag coefficients presented in previous analyses [15,16]. The assumption of this uniform distribution indicates the current poor state of knowledge of the actual distribution of drag coefficients for unknown orbiting objects. The uniform PDF yields a mean of  $\bar{C}_{D,j} = (C_{D,\max} + C_{D,\min})/2 = 2.5$  and variance  $\sigma_{C_{D,j}}^2 = (C_{D,\max} - C_{D,\min})^2/12 = 0.053$  (i.e.,  $\sigma_{C_{D,j}} = 0.23$ ).

In summary, estimating LEO satellite RCS+BC masses requires several assumptions and approximations:

- 1) The RCS+BC mass estimation method assumes that correlations between  $A_j$ ,  $B_j$ , and  $C_{D,j}$  can be neglected.
- 2) The method roughly approximates atmospheric drag projected areas as  $A_j \approx (\pi D_j^2/4)$ .
- 3) The method assumes a lognormal distribution for the uncertainty PDF of inverse ballistic coefficient, based on empirically determined means and variances.
- 4) The method assumes a uniform distribution for the drag coefficient PDF.

As described in the following, the combined effects of these assumptions and approximations significantly limit the accuracy of the mass calibration and estimation processes.

## B. Calibrating RCS+BC Mass Estimation Process

The mass calibration process uses box-shaped DISCOS satellites, as described previously for the HBR calibration process. For the calibration epoch date of 15 January 2022, sufficient RCS data and VCM BC estimates are available for  $J = 554$  of these satellites. Each provides an independent (albeit noisy) measurement of the logarithmic calibration factor,  $\psi_j = \ell_n[M_j^K / (A_j B_j C_{D,j})]$ , yielding combined estimates of

$$\bar{\psi} = \frac{1}{J} \sum_{j=1}^J \psi_j \text{ and } \sigma_{\psi}^2 = \frac{1}{J-1} \sum_{j=1}^J [\psi_j - \bar{\psi}]^2 \quad (27)$$

derived by applying the same Bayesian method [31] used for the HBR calibration process. For the 15 January 2022 calibration data, the analysis yields  $\bar{\psi} = -0.159$  and  $\sigma_{\psi} = 0.959$ , corresponding to a mean linear calibration factor of  $\bar{\Psi} = I_1(\bar{\psi}, \sigma_{\psi}) = 1.35$ . The estimated  $\sigma_{\psi}$  value indicates significant satellite-to-satellite variation among the calibration satellites.

To assess the accuracy of the calibrated estimation process, Fig. 4 compares the CDF of the ratio of statistically expected calibrated RCS+BC mass estimates  $\bar{M}_j$  to the known masses  $M_j^K$  for the 554 satellites. (Sec. IV.D explains how the  $\bar{M}_j$  values are calculated.) The CDF indicates that, among this population, calibration uncertainties limit the 90% confidence accuracy range of the estimation process to

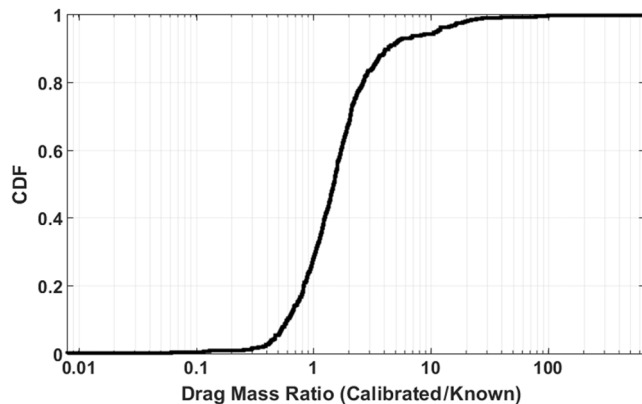


Fig. 4 CDF of the ratio of calibrated RCS+BC mass estimates to known masses for 554 satellites.

within a factor of 0.47 for potential mass underestimations and to within a factor of 10.9 for potential mass overestimations.

## C. Estimating RCS- and SRPC-Based Mass for LEO Objects Experiencing Solar Radiation Pressure

Combining RCS-based size estimates and OD-based solar radiation pressure coefficient estimates provides a means to estimate the masses of satellites that experience measureable SRP perturbations. This RCS+SRPC mass estimation analysis approximates the characteristic mass of a LEO satellite using an expression similar in form to that used for RCS+BC-based mass estimation given by Eq. (18),

$$\mathcal{M}_{R,j} \approx (\pi D_j^2/4) G_j C_{R,j} \quad (28)$$

In this expression,  $\mathcal{M}_{R,j}$  indicates the mass that characterizes SRP perturbations experienced by the  $j$ th satellite, which is proportional to the product of three quantities: the area projected toward the incident sunlight (again approximated using  $\pi D_j^2/4$ ), the inverse solar radiation pressure coefficient  $G_j$ , and the reflectivity coefficient  $C_{R,j}$  (see Ref. [25] for more details on orbital SRP perturbations). As before, this study introduces a positive scalar calibration factor  $\Theta_j$  into Eq. (28) to quantify the bias and uncertainty of the RCS+SRPC mass estimation process

$$M_j \approx \Theta_j \mathcal{M}_{R,j} = e^{\theta_j} [(\pi D_j^2/4) G_j C_{R,j}] \quad (29)$$

with  $M_j$  indicating the calibrated mass of the satellite,  $\Theta_j$  indicating the linear calibration factor, and  $\theta_j$  indicating the logarithmic calibration factor. Once again, analysis indicates that the observed distribution of the logarithmic  $\theta_j$  factors matches a Gaussian distribution significantly better than that of the linear  $\Theta_j$  factors. The process of estimating the calibration factors for the RCS+SRPC mass estimation process uses the same exact analysis steps as outlined in the previous sections for the RCS+BC mass estimation process but substituting the OD-based inverse solar radiation pressure coefficient  $G_j$  for the inverse ballistic coefficient  $B_j$  and also substituting the reflectivity coefficient  $C_{R,j}$  for the drag coefficient  $C_{D,j}$ . (This study considers SRP effects not to be measurable if none of the available VCMs provides a usable, positive-valued  $G_j$  coefficient, which can occur for low-altitude satellites.) The analysis assumes a uniform reflectivity coefficient PDF with bounds  $C_{R,\min} = 1$  and  $C_{R,\max} = 1.4$  for all satellites, which yields a mean of  $\bar{C}_{R,j} = 1.2$ , and variance  $\sigma_{C_{R,j}}^2 = 0.013$  (i.e.,  $\sigma_{C_{R,j}} = 0.12$ ). The lower bound of  $C_{R,\min} = 1$  corresponds to that expected for dark bodies (i.e., that have negligible overall reflectance) of any shape. The upper bound of  $C_{R,\max} = 1.4$  represents the theoretical value for a Lambertian sphere with 90% reflectance [34] and is assumed to provide a reasonable upper limit for unknown secondary objects. The assumption of this uniform distribution indicates the current poor state of knowledge of the actual distribution of reflectivity coefficients for unknown orbiting objects.

The analysis restricts RCS+SRPC mass estimation to satellites with perigee altitudes above 450 km altitude, in order to ensure that imperfectly modeled atmospheric drag perturbations do not bias the solar radiation pressure coefficients estimated in the OD analysis, which has been observed to occur for LEO satellites at lower altitudes. For the calibration epoch date of 15 January 2022, sufficient RCS data and VCM SRPC estimates are available for  $J = 303$  of the DISCOS cuboid satellites with perigees above 450 km altitude. The analysis yields  $\bar{\theta} = 0.173$  and  $\sigma_{\theta} = 0.884$  and a mean linear calibration factor of  $\bar{\Theta} = I_1(\bar{\theta}, \sigma_{\theta}) = 1.76$ .

To assess the accuracy of the calibrated estimation process, Fig. 5 compares the CDF of the ratio of statistically expected calibrated RCS+SRPC mass estimates  $\bar{M}_j$  to the known masses  $M_j^K$  for the 303 satellites. (Sec. IV.D explains how the  $\bar{M}_j$  values are calculated.) The CDF indicates that, among this population, calibration uncertainties limit the 90% confidence accuracy range of the RCS+SRPC mass estimation process to within a factor of 0.44 for potential underestimations and to within a factor of 5.6 for potential overestimations.



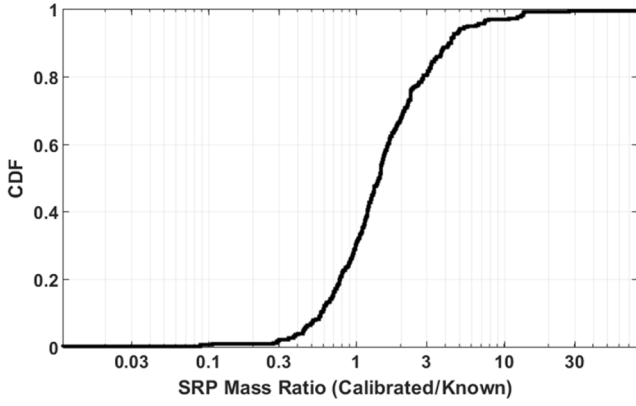


Fig. 5 CDF of the ratio of calibrated RCS+SRPC mass estimates to known masses for 303 satellites.

This means that, for satellites with perigee altitudes above 450 km, the RCS+SRPC method provides somewhat more accurate mass estimates than the RCS+BC estimation method, because it produces a comparable number of mass underestimates, but significantly fewer number of large-amplitude overestimates.

#### D. Estimating Statistically Expected Masses

Estimating a satellite's statistically expected mass using the RCS+BC method results in a four-dimensional expectation value integral that has the following analytical approximation:

$$\bar{M}_j \approx \mathbb{E}[e^{\psi_j} (A_j B_j C_{D,j})] \approx I_1(\bar{\psi}, \sigma_\psi) [\bar{A}_j \bar{B}_j \bar{C}_{D,j}] \quad (30)$$

This expected value averages over a set of four random variables,  $\{D_j, \psi_j, B_j, C_{D,j}\}$ , and accounts in an approximate way for the combined uncertainties of these quantities. The associated variance also has an analytical approximation,

$$\sigma_{M_j}^2 \approx I_2(\bar{\psi}, \sigma_\psi) \left[ (\bar{A}_j^2 + \sigma_{A_j}^2) (\bar{B}_j^2 + \sigma_{B_j}^2) (\bar{C}_{D,j}^2 + \sigma_{C_{D,j}}^2) \right] - \bar{M}_j^2 \quad (31)$$

with  $\bar{A}_j = \pi(\bar{D}_j^2 + \sigma_{D_j}^2)/4$  and  $\sigma_{A_j}^2 = [\pi^2(\sum_n D_{j,n}^4)/(16N_j^{\text{RCS}})] - (\bar{A}_j)^2$ . The corresponding equations for the RCS+SRPC method have the same exact form, after substituting the inverse solar radiation pressure coefficient  $G_j$  for the inverse ballistic coefficient  $B_j$  and the reflectivity coefficient  $C_{R,j}$  for the drag coefficient  $C_{D,j}$  and so on. This means that the RCS+SRPC method accounts for the combined uncertainties of the four quantities  $\{D_j, \theta_j, G_j, C_{R,j}\}$ .

For satellites with perigee altitudes above 450 km that also have solar radiation pressure coefficient data available, this analysis uses the RCS+SRPC method to provide best estimate masses and uncertainties. For other satellites that have ballistic coefficient data available, the analysis uses the RCS+BC method. Figure 6 shows the distribution of the resultant secondary statistically expected masses (i.e.,  $\bar{M}_2$ ) for the 225,695 known-on-unknown CARA conjunctions that have sufficient RCS and OD data to allow size and mass estimation. The CDF indicates a median  $\bar{M}_2$  value of 0.1 kg and a central 90% range of  $8.1 \text{ g} \leq \bar{M}_2 \leq 4.2 \text{ kg}$ . Notably, only about 2.8% of the studied conjunctions involves secondary objects with  $\bar{M}_2 > 10 \text{ kg}$ , and less than 1% has  $\bar{M}_2 > 100 \text{ kg}$ .

#### V. Estimating Collision Probabilities for Conjunctions Involving Unknown Objects

The probability of collision for a conjunction involving two known satellites depends on their combined hard-body radii,  $P_c(R) = P_c(R_1 + R_2)$ . If no auxiliary variables are required for collision probability estimation (as discussed in Sec. III.A), then calculation of the  $P_c(R)$  function requires two-dimensional (2D) numerical inte-

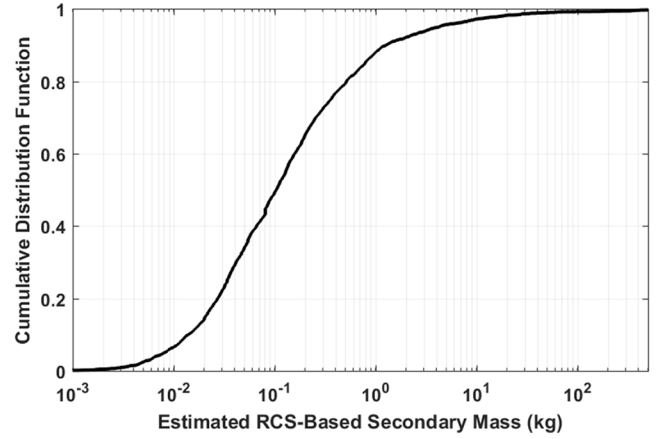


Fig. 6 The distribution of RCS-based statistically expected masses for secondary objects involved in known-on-unknown CARA conjunctions processed from 1 September 2020 to 30 June 2021.

gration for most conjunctions [3,4] or three-dimensional (3D) numerical integration for a relatively small remaining set, which includes low relative velocity encounters [7]. Alternatively, the  $P_c(R)$  function can be approximated using multiterm series expansions [5,35], which trade numerical estimation accuracy for increased efficiency. All of the analyses in this study calculate the  $P_c(R)$  function using the 2D numerical integration method of Foster and Estes [3].

For single  $P_c(R)$  calculations, such as those required for known-on-known conjunctions, computational efficiency unlikely represents a prohibitive limit when evaluating the  $P_c(R)$  function, except perhaps when using the 3D numerical integration method [7] or methods that require auxiliary variables (e.g., Refs. [18,19,21,22]). However, for conjunctions that involve one or two unknown objects, explicitly computing statistically expected collision probabilities usually requires many  $P_c(R)$  function evaluations, which can become computationally demanding. This section develops expressions that provide the means to calculate  $\bar{P}_c$  using accurate explicit computation, along with methods to approximate  $\bar{P}_c$  more efficiently.

#### A. Collision Probability Estimation Using RCS-Based Size Distributions

For a known-on-unknown conjunction, calculating  $\bar{P}_c$  requires 2D integration to account for uncertainties in the secondary object's RCS-based characteristic size  $D_2$  and the associated HBR calibration factor  $\omega_2$  as

$$\bar{P}_c = \mathbb{E}[P_c(R_1^K + R_2)] = \mathbb{E}[P_c(R_1^K + e^{\omega_2} D_2/2)] \quad (32)$$

$$= \int_0^\infty \rho(D_2) \left\{ \int_{-\infty}^\infty \rho(\omega_2) [P_c(R_1^K + e^{\omega_2} D_2/2)] d\omega_2 \right\} dD_2 \quad (33)$$

with  $R_1^K$  indicating the primary's known HBR. Inserting the empirical PDF  $\rho(D_2)$  of Eq. (5) yields a summation,

$$\bar{P}_c = \frac{1}{N_2^{\text{RCS}}} \sum_{n=1}^{N_2^{\text{RCS}}} \left\{ \int_{-\infty}^\infty \rho(\omega_2) [P_c(R_1^K + e^{\omega_2} D_{2,n}/2)] d\omega_2 \right\} \quad (34)$$

Evaluating the  $\omega_2$  integral numerically using Gauss–Hermite (GH) quadrature [36] yields a double summation,

$$\bar{P}_c = \frac{1}{N_2^{\text{RCS}}} \sum_{n=1}^{N_2^{\text{RCS}}} \sum_{u=1}^{N_{\text{GH}}} w_u P_c(R_1^K + e^{\omega_{2,u}} D_{2,n}/2) \quad (35)$$

with  $w_u$  indicating the GH quadrature weights and  $\omega_{2,u}$  indicating the associated quadrature points. Equation (35) contains a total of  $N_2^{\text{RCS}} \times N_{\text{GH}}$  summation terms, each of which requires one computation of the  $P_c(R)$  function. Experience indicates that achieving reasonable

numerical integration accuracy requires  $N_{GH} \geq 16$ . Because  $N_2^{RCS}$  often exceeds approximately 1,000 for well-observed objects, calculating the summation in Eq. (35) requires approximately 16,000 or more  $P_c(R)$  function computations. This indicates that calculating  $\bar{P}_c$  using explicit summation for known-on-unknown conjunctions requires significant (but often still manageable) computation. However, the calculation grows substantially for unknown-on-unknown conjunctions, which each require a quadruple summation,

$$\bar{P}_c = \frac{1}{N_1^{RCS} N_2^{RCS}} \sum_{n=1}^{N_1^{RCS}} \sum_{m=1}^{N_2^{RCS}} \sum_{u=1}^{N_{GH}} \sum_{v=1}^{N_{GH}} w_u w_v P_c \left( \frac{e^{\omega_{1,u}} D_{1,n} + e^{\omega_{2,v}} D_{2,m}}{2} \right) \quad (36)$$

containing approximately 256 million or more terms and associated  $P_c(R)$  function computations. Because calculating this summation explicitly may potentially represent an unmanageable level of computation, Secs. V.D, V.F, and V.H discuss methods to approximate  $\bar{P}_c$  values more efficiently.

### B. Performance of RCS-Based Collision Probability Estimation

As discussed previously in Sec. III.E, the special set of conjunctions involving known small secondary objects provides a means of testing how well RCS-based estimation performs. Figure 7 compares collision probabilities for these 33,371 small-secondary conjunctions. The horizontal axis plots collision probabilities calculated using the known hard-body radii, in other words,  $P_c^K = P_c(R_1^K + R_2^K)$ . The vertical axis of the top panel plots RCS-based  $\bar{P}_c$  estimates calculated using Eq. (35). The vertical axis of the bottom panel plots the ratio  $\bar{P}_c/P_c^K$ . For CARA red-level conjunctions with collision probabilities greater than or equal to  $10^{-4}$ , the RCS-based estimates and known-HBR estimates all agree to within 10%. As discussed previously, this relatively accurate agreement occurs because many CARA primary objects have HBRs that are much larger than the secondary HBRs. However, Fig. 7 indicates that a small number of discrepancies of a factor of 1.5 or more occur among conjunctions with smaller collision probabilities; notably, in all of these cases, the RCS-based collision probabilities overestimate the known-HBR collision probabilities.

### C. Collision Probabilities Estimated for CARA Conjunctions

As mentioned previously, the CARA processing system currently uses a fixed, default HBR value of 1.5 m for all unknown secondary objects. (Note that CARA adopted this default value based on an internal analysis conducted in 2014, which used median RCS values as input to the NASA SEM and indicated that about 99% of debris have

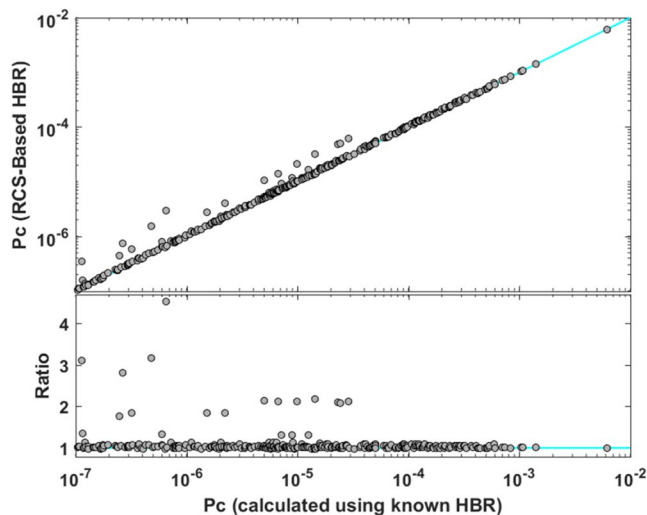


Fig. 7 Collision probabilities for CARA conjunctions involving small secondary objects. The horizontal axes plot probabilities calculated using known HBR values  $P_c^K$ . The vertical axis of the top panel plots RCS-based expected probabilities  $\bar{P}_c$ , and the bottom panel plots the  $\bar{P}_c/P_c^K$  ratio.

characteristic sizes  $D_j \leq 3$  m, leading to the adoption of  $R_j = 1.5$  m as a conservatively large value to use for all unknown secondary objects.) Figure 8 compares collision probabilities estimated for the 225,695 known-on-unknown CARA conjunctions that have sufficient auxiliary RCS and OD data to allow secondary object size and mass estimation. The top panel of Fig. 8 plots probabilities calculated using a secondary HBR of 1.5 m on the vertical axis vs probabilities calculated neglecting the secondary HBR on the horizontal axis, in other words,  $P_c(R_1^K + 1.5 \text{ m})$  vs  $P_c(R_1^K)$ . Each plotted point represents one conjunction. As would be expected, adding a secondary HBR of 1.5 m increases all of the probabilities, and the CDF plotted as the dashed curve in the bottom panel shows the distribution of the  $P_c(R_1^K + 1.5 \text{ m})/P_c(R_1^K)$  ratios for all conjunctions with  $P_c(R_1^K) > 10^{-7}$ .

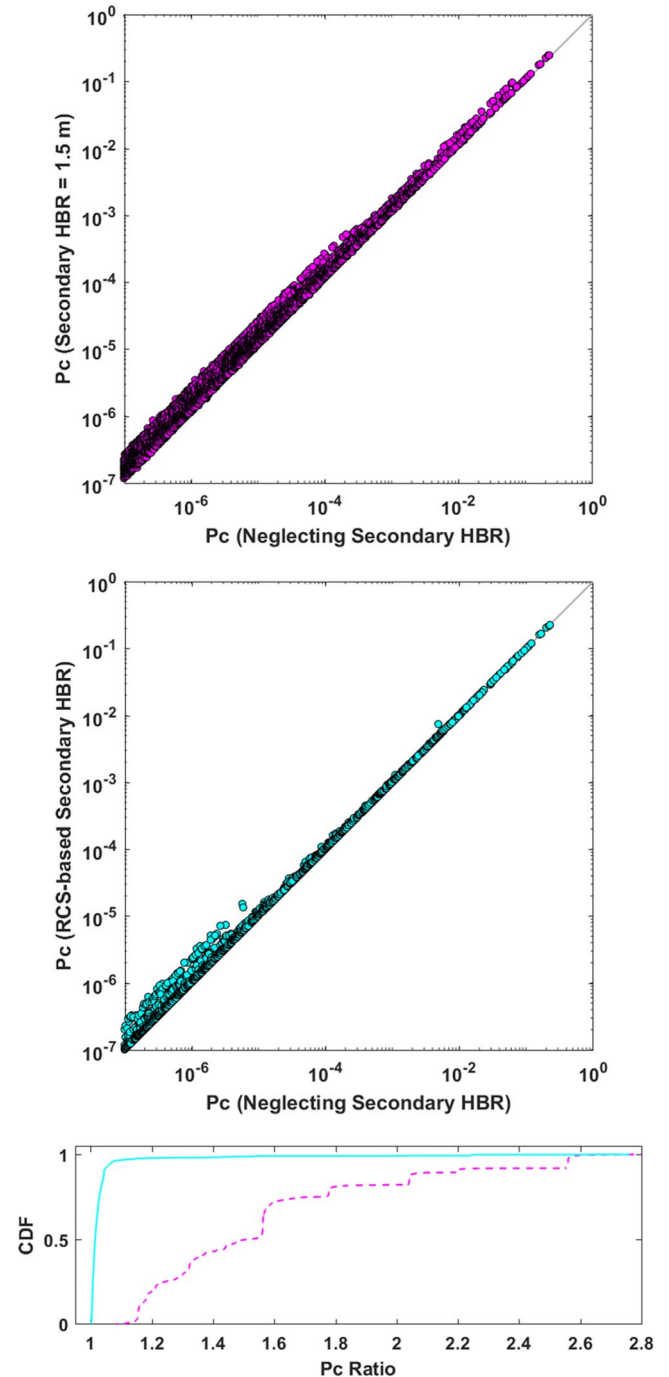


Fig. 8 Collision probabilities for known-on-unknown CARA conjunctions calculated using a fixed secondary object HBR of 1.5 m (top) and using RCS-based HBR estimates (middle). The bottom panel compares CDFs of the ratio of the probabilities calculated including and neglecting secondary HBR values.

The middle panel of Fig. 8 plots RCS-based expected probabilities calculated using Eq. (35) vs probabilities calculated neglecting the secondary HBR, in other words,  $\bar{P}_c$  vs  $P_c(R_1^K)$ , and the CDF plotted as the solid curve in the bottom panel shows associated  $P_c$  ratio. The distribution of resulting probabilities differs significantly for the two methods and indicates that, for most CARA conjunctions, the RCS-based estimation method leads to significantly smaller collision probabilities than using the fixed-HBR method. For instance, as shown in the bottom panel of Fig. 8, the fixed-HBR approach increases collision probabilities by a factor of 1.5 or more for over 50% of the plotted conjunctions, but the RCS-based method increases probabilities by a factor of greater than or equal to 1.5 for less than 1%.

Among the 225,695 known-on-unknown conjunctions analyzed in this study, using the fixed-HBR method produces 2010 *red-level* CARA events (i.e., those with estimated collision probabilities greater than or equal to  $10^{-4}$ ), whereas the RCS-based method yields 1734 *red-level* events, a reduction of 14%. Similarly, the fixed-HBR method produces 12,257 events with probabilities greater than or equal to  $10^{-7}$  (i.e., above the *yellow-level* threshold) compared to 11,635 RCS-based events, a reduction of 5%. This means that adopting the RCS-based estimation approach should lead to a modest reduction in the overall number of yellow- and red-level conjunctions processed by the CARA system.

#### D. Monte Carlo Collision Probability Estimation

The MC integration method [36] often requires significantly less computation than direct summation to calculate sufficiently accurate  $\bar{P}_c$  estimates, especially for unknown-on-unknown conjunctions. For an unknown-on-unknown conjunction, MC integration entails sampling the four PDFs,  $\rho(D_1)$ ,  $\rho(D_2)$ ,  $\rho(\omega_1)$ , and  $\rho(\omega_2)$  and averaging over the sampled set as

$$\bar{P}_c \approx \text{mean}(P'_{c,s}) = \frac{1}{N_s} \sum_{s=1}^{N_s} P_c \left( \frac{e^{\omega'_{1,s}} D'_{1,s} + e^{\omega'_{2,s}} D'_{2,s}}{2} \right) \quad (37)$$

with  $N_s$  indicating the total number of samples,  $P'_{c,s}$  indicating the probability calculated for each sample, and  $\{D'_{1,s}, D'_{2,s}, \omega'_{1,s}, \omega'_{2,s}\}$  indicating the sampled characteristic sizes and calibration factors of the primary and secondary objects, respectively. (Note that primes denote sampled values, so  $\omega'_{1,s}$  represents the  $s$ th sample of the random variable  $\omega_1$ ,  $P'_{c,s}$  represents the probability calculated for the  $s$ th sample, etc.) Generating the  $D'_{j,s}$  samples entails randomly drawing indices  $n_s$  from the discrete set of integers  $\{1 \dots N_j^{\text{RCS}}\}$  using the sampling-with-replacement method (e.g., with MATLAB®'s `randi` function) and setting  $D'_{j,s} = D_{j,n_s}$ . Generating the  $\omega'_{j,s}$  samples entails calculating random deviates  $z_s$  of the standard normal function (e.g., with MATLAB®'s `randn` function; also see Ref. [36]) and setting  $\omega'_{j,s} = \bar{\omega}_j + z_s \sigma_{\omega_j}$ . The 1-sigma MC estimation uncertainty for  $\bar{P}_c$  corresponds to the standard deviation of the mean [36]

$$\sigma_{\bar{P}_c} = \frac{\text{std}(P'_{c,s})}{\sqrt{N_s}} = \left[ \frac{1}{N_s(N_s - 1)} \sum_{s=1}^{N_s} (P'_{c,s} - \bar{P}_c)^2 \right]^{1/2} \quad (38)$$

which tends to decrease in proportion to  $1/\sqrt{N_s}$ . This expression enables iteratively increasing the number of samples in order to achieve a desired estimation accuracy.

Achieving a desired estimation accuracy of  $\sigma_{\bar{P}_c}/\bar{P}_c \approx 1\%$  (more than sufficient for conjunction risk assessments) usually requires significantly fewer  $P_c(R)$  function computations than explicitly calculating the summations in Eq. (35) or Eq. (36). Specifically, among the 225,695 known-on-unknown CARA conjunctions analyzed in this study, fewer than 1% were found to require more than  $10^4$  samples to achieve or exceed this desired accuracy, and about 0.4% required greater than  $10^5$  samples.

#### E. Monte Carlo Collision Probability Quantiles

Sorting sample probabilities into increasing order allows the estimation of MC probability quantiles  $P_Q$ , which provide more or less

conservative confidence estimates of collision risk, depending on the quantile value  $Q$ . Specifically, the conservative 99% quantile with  $Q = 0.99$  is given by  $P_Q \approx P'_{s_Q}$  with the MC sample index  $s_Q = QN_s$  rounded up to the next largest integer. However, for collision probabilities that depend on uncertain auxiliary variables, such as those contained in the vector  $\mathbf{a}$  described in Sec. II.A, additional sampling is required to estimate overall confidence quantiles. Specifically, in these cases, estimating the 99% quantile requires an MC sampling algorithm that accounts for uncertainties in  $\mathbf{a}$ , in addition to uncertainties in  $R_1$  and  $R_2$ . This method of accounting for uncertainties in auxiliary variables is an ongoing subject of CARA research.

#### F. Effective Hard-Body Radius Collision Probability Approximation

Series expansion analysis indicates that  $P_c(R) \propto R^2$  for sufficiently small combined hard-body radii [35]. In practice, this *small-HBR limit* applies to conjunctions in which  $R$  is much smaller than all other relevant length scales (e.g., smaller than both conjunction plane miss distances and both covariance sigma values as described by Alfano [37]). Let  $R_e$  denote the *effective* combined HBR, defined using the following relationship:  $\bar{P}_c = P_c(R_e)$ . For conjunctions that satisfy the small-HBR limit,  $P_c(R) \approx P_c(R/R_e)^2$ , and the collision probability for an unknown-on-unknown conjunction has the approximate analytical solution

$$\bar{P}_c = \mathbb{E}[P_c(R)] \approx \frac{P_e}{R_e^2} [(\bar{R}_1 + \bar{R}_2)^2 + \sigma_{R_1}^2 + \sigma_{R_2}^2] \quad (39)$$

which indicates that the effective HBR is approximately

$$R_e \approx \sqrt{(\bar{R}_1 + \bar{R}_2)^2 + \sigma_{R_1}^2 + \sigma_{R_2}^2} \quad (40)$$

In other words, for conjunctions that satisfy the small-HBR limit, the  $\bar{P}_c$  value is approximately

$$\bar{P}_c \approx P_c \left( \sqrt{(\bar{R}_1 + \bar{R}_2)^2 + \sigma_{R_1}^2 + \sigma_{R_2}^2} \right) \quad (41)$$

This is the most computationally efficient means of approximating  $\bar{P}_c$  formulated in this analysis because it only requires one  $P_c(R)$  function computation. The approximation also applies to known-on-unknown conjunctions, by substituting the known HBR for  $\bar{R}_1$  and setting  $\sigma_{R_1}$  equal to 0.

Figure 9 compares  $\bar{P}_c$  values estimated for the known-on-unknown CARA conjunctions calculated using Eq. (35) to those

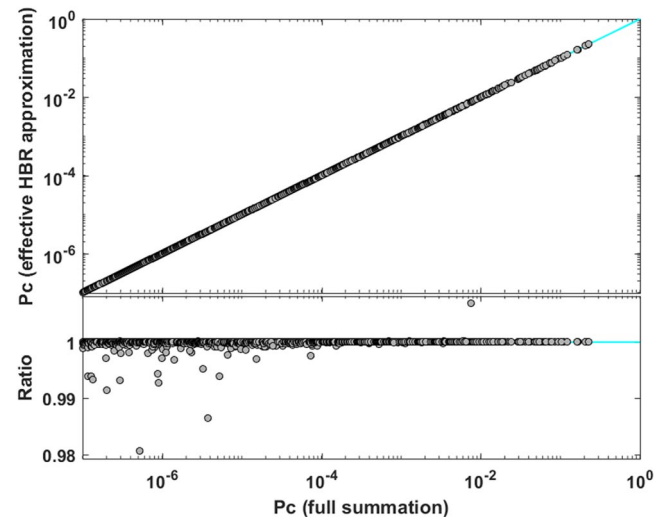


Fig. 9 Collision probabilities for known-on-unknown CARA conjunctions calculated using explicit summation (horizontal axis) compared to those calculated using the effective-HBR approximation (vertical axis of top panel). The approximation is accurate to within 1% for the vast majority of examined cases.

approximated using the effective-HBR approximation of Eq. (41). In this case, the approximation is accurate to within 2% for all of the 11,635 plotted cases with  $\bar{P}_c \geq 10^{-7}$ . However, preliminary simulation analysis indicates that the effective-HBR approximation potentially could be less accurate for some unknown-on-unknown conjunctions, specifically those with comparable primary and secondary HBR sizes. For these cases, the MC method provides an accurate means of probability approximation.

### G. Steep-Growth Hard-Body Radius Collision Probability Approximation

For conjunctions that do not satisfy the small-HBR limit, the  $P_c(R)$  curve can grow more or less steeply than the  $P_c(R) \propto R^2$  trend. For instance, in the large-HBR limit, as  $R \rightarrow \infty$ , growth slows significantly because  $P_c \rightarrow 1$ . For  $R$  values that moderately exceed the small-HBR limit, a higher-order series expansion analysis [35] indicates that  $P_c(R) \approx aR^2 + bR^4$ , and numerical studies indicate that the growth can approach or even exceed a  $P_c(R) \propto R^4$  trend in some cases. To investigate this steep-growth scenario, consider a conjunction for which  $P_c(R) \propto R^g$  with  $g \approx 4$ . This implies that  $\bar{P}_c \approx P_c(R_g)$ , with the steep-growth combined HBR given by

$$R_g^4 = \mathbb{E}[(R_1 + R_2)^4] \\ = \mathbb{E}[R_1^4] + 4\mathbb{E}[R_1^3]\mathbb{E}[R_2] + 6\mathbb{E}[R_1^2]\mathbb{E}[R_2^2] \\ + 4\mathbb{E}[R_1]\mathbb{E}[R_2^3] + \mathbb{E}[R_2^4] \quad (42)$$

The expected values required to calculate  $R_g$  have the form  $\mathbb{E}[R_j^q] = I_q(\bar{\omega}, \sigma_\omega) \left\{ \left[ \sum_n (D_{j,n}/2)^q \right] / N_j^{\text{RCS}} \right\}$  and can be precalculated and tabulated for computational efficiency. Equation (42) also applies to known-on-unknown conjunctions by substituting  $\mathbb{E}[R_j^q] = (R_j^K)^q$ . Analysis indicates that 97% of the studied CARA known-on-unknown conjunctions have growth exponents of 4 or less (i.e.,  $g \leq 4$ ) in the region of the  $P_c(R)$  curve that contributes most to the expected value calculation. Notably, for all conjunctions involving unknown objects, the steep-growth probability estimate exceeds the effective-HBR probability estimate, in other words,  $P_c(R_g) > P_c(R_e)$ .

### H. Efficient Screening Using Effective-HBR and Steep-Growth Approximations

The effective-HBR and steep-growth approximations provide an efficient and reliable means of screening conjunctions, in order to test if a more computationally intensive method is required to calculate  $\bar{P}_c$  estimates. For instance, this specific study aims to analyze in detail all yellow- or red-level conjunctions with  $\bar{P}_c \geq 10^{-7}$ . To determine conservatively if a conjunction's  $\bar{P}_c$  could potentially be larger than this threshold, the analysis first calculates the steep-growth approximation and compares  $P_c(R_g)$  to a screening value of  $10^{-10}$  (i.e., a green-level threshold that is three orders of magnitude smaller than the yellow-level threshold). If  $P_c(R_g) < 10^{-10}$ , which is the case for a large majority of CARA conjunctions, then the analysis uses the effective-HBR method to estimate the collision probability, in other words,  $\bar{P}_c \approx P_c(R_e)$ , which is itself also guaranteed to be less than the green-level threshold. Otherwise, the analysis calculates  $\bar{P}_c$  more accurately using the explicit summation or MC approaches, as described previously. Testing indicates that the three-orders-of-magnitude separation between green- and yellow-level probabilities used in the screening process is more than adequate to ensure identification and accurate processing of all actual yellow- and red-level known-on-unknown conjunctions. Preliminary analysis indicates that a three-orders-of-magnitude separation also suffices for unknown-on-unknown conjunctions.

## VI. Estimating Fragmentation Risks for Conjunctions Involving Unknown Objects

This section formulates two metrics to assess fragmentation risks to the orbital environment: the statistically expected number of trackable fragments produced during a conjunction and the proba-

bility of producing more than a threshold number of trackable fragments. Both use the EVOLVE fragmentation model [17] given by Eq. (3), which approximates  $F_{\text{EV}}(M_1, M_2)$ , the number of trackable fragments produced if a collision were to occur during a conjunction.

### A. Statistically Expected Number of Fragments

For a known-on-known conjunction, multiplying the collision probability by  $F_{\text{EV}}(M_1, M_2)$  equals the number of trackable fragments statistically expected to be produced, in other words,  $F_c(R_1, R_2, M_1, M_2) \approx P_c(R_1 + R_2) \times F_{\text{EV}}(M_1, M_2)$ , which is calculated using the known HBRs and masses of the two objects. For conjunctions involving unknown objects, the statistically expected number of fragments accounts for size and mass uncertainties by averaging over all relevant random variables

$$\bar{F}_c = \mathbb{E}[F_c(R_1, R_2, M_1, M_2)] \approx \mathbb{E}[P_c(R_1 + R_2) \times F_{\text{EV}}(M_1, M_2)] \quad (43)$$

For known-on-unknown conjunctions, calculating this expectation value represents integrating over a set of five random variables that account for the size and mass estimation uncertainties of the secondary object. Specifically, for the RCS+BC mass estimation method, these five random variables are  $\{D_2, \omega_2, \psi_2, B_2, C_{D,2}\}$ ; for RCS+SRPC mass estimation, they are  $\{D_2, \omega_2, \theta_2, G_2, C_{R,2}\}$ . Correspondingly, unknown-on-unknown collisions require integrations over ten random variables accounting for the estimation uncertainties of both objects. In other words, estimating the statistically expected number of trackable fragments  $\bar{F}_c$  entails evaluating either a five- or ten-dimensional integral. The integrand function of these multidimensional integrals contains the product of the conjunction's collision probability  $P_c(R_1 + R_2)$ , and the estimated number of fragments given that a collision occurs,  $F_{\text{EV}}(M_1, M_2)$ . Both of these functions are nonlinear, and the latter also possesses discontinuities. The Monte Carlo method [36] provides an efficient and straightforward means of computing such multidimensional integrals.

### B. Probability of Exceeding Threshold Number of Trackable Fragments

A conjunction's probability of producing more than a threshold number of trackable fragments  $F$  is given by

$$\bar{P}_F = \mathbb{E}[P_F(R_1, R_2, M_1, M_2)] \\ \approx \mathbb{E}[P_c(R_1 + R_2) \times U(F_{\text{EV}}(M_1, M_2) - F)] \quad (44)$$

which is referred to as the *fragmentation probability* in this study, for brevity. In this case, the integrand is the product of the collision probability and the binary probability that the number of fragments  $F_{\text{EV}}(M_1, M_2)$  exceeds the specified threshold value  $F$ . Again, the MC integration method provides an efficient means of computing  $\bar{P}_F$ .

For  $F = 0$ , it is straightforward to show that  $\bar{P}_F = \bar{P}_c$ . More generally, a conjunction's fragmentation probability cannot exceed the collision probability, in other words,  $\bar{P}_F \leq \bar{P}_c$ . For groups like CARA that use the collision probability to assess mission risks, this inequality property makes  $\bar{P}_F$  a convenient choice to assess environmental risks for two reasons. First, the efficient conjunction screening method for  $\bar{P}_c$  (described in Sec. V.H) also applies to  $\bar{P}_F$  without modification. Specifically, if the screening process indicates that  $\bar{P}_c$  is less than a negligibly small green-level cutoff, then  $\bar{P}_F$  also must be less than that cutoff, which efficiently eliminates the need to calculate either  $\bar{P}_c$  or  $\bar{P}_F$  more accurately. Second, the inequality implies that all conjunctions that represent red-level environmental risks (i.e., those with  $\bar{P}_F \geq 10^{-4}$ ) are naturally contained within the set of conjunctions identified as red-level mission risks (i.e., those with  $\bar{P}_c \geq 10^{-4}$ ).

To demonstrate how collision and fragmentation probabilities can be used together, this study uses a fragment production threshold of  $F = 10^3$  to assess an unacceptably high level of risk to the orbital environment. Figure 10 compares fragmentation and collision probabilities for the known-on-unknown CARA conjunctions, calculated



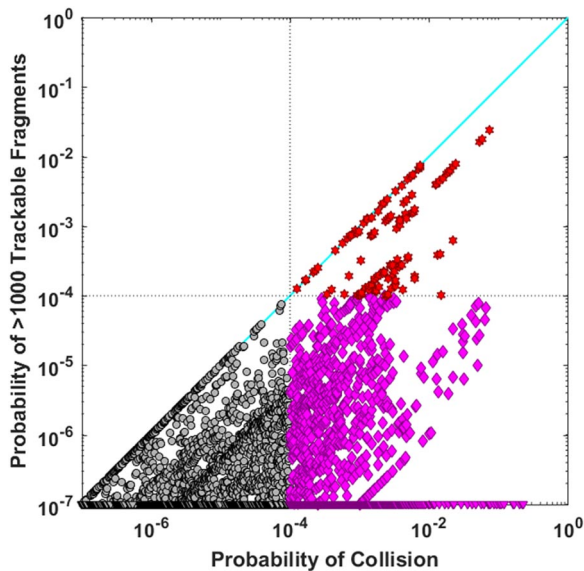


**Fig. 10** Collision and fragmentation probabilities for known-on-unknown conjunctions. The horizontal axis plots RCS-based collision probabilities. The vertical axis plots the probability of producing more than 1000 trackable fragments. Red stars indicate conjunctions with high mission and environmental risks. Pink diamonds indicate those with high mission risk but lower environmental risks. Downward pointing triangles indicate upper-limit values.

using this threshold. Among the original 225,695 known-on-unknown CARA conjunctions, 1734 represent red-level mission risks with  $\bar{P}_c \geq 10^{-4}$ . Among these, 122 (or 7%) also have  $\bar{P}_F \geq 10^{-4}$ , so they represent red-level environmental risks as well. Figure 10 plots these dual high-risk conjunctions as red stars, illustrating how collision and fragmentation probabilities can be used together to identify the subset of events with the highest mission and environmental risks. Pink diamonds and triangles represent conjunctions with red-level mission risks but lower environmental risks.

As discussed previously, a fragment production threshold of  $F = 10^3$  indicates that 7% of the analyzed known-on-unknown conjunctions with  $\bar{P}_c \geq 10^{-4}$  also have  $\bar{P}_F \geq 10^{-4}$ . This analysis uses  $F = 10^3$  as a threshold number of trackable fragments because such a collision would potentially represent a major source of debris generation, roughly comparable to the Iridium-Cosmos collision in 2009 which produced about 1200 tracked fragments that remained in Earth orbit for longer than one year [13]. Other production thresholds provide different assessments of environmental risk in a nonlinear fashion. For instance, about 20% of the studied conjunctions have  $\bar{P}_F \geq 10^{-4}$  for the somewhat more moderate threshold of  $F = 10^2$ . So, considering the range of  $10^2 \leq F \leq 10^3$  indicates that 7 to 20% of the high mission risk conjunctions also could be assessed to pose an elevated risk to the orbital environment.

## VII. Conclusions

The methods formulated in this study to estimate RCS-based sizes and masses provide the means to approximate collision and fragmentation probabilities for conjunctions involving unknown satellites. The methodology uses ensembles of RCS measurements to estimate calibrated hard-body radii, along with the associated uncertainty distributions. The size calibration analysis indicates that RCS-based HBR estimates are accurate at the 90% confidence level to within a factor of 0.59 for potential underestimations to 3.1 for potential overestimations.

Collision probabilities calculated as statistical expectation values naturally account for HBR estimation uncertainties inferred from the distribution of RCS measurements and the scatter of the calibration comparisons. Several methods enable computation of collision probabilities involving unknown objects. These include the explicit summation methods of Eq. (35) or Eq. (36) as well as the more

efficient Monte Carlo, effective-HBR, and steep-growth approximation methods. Specifically, the effective-HBR approximation given by Eq. (41) provides a particularly computationally efficient means to estimate collision probabilities involving satellites with uncertain hard-body radii, with sufficient accuracy required for typical conjunction risk assessments.

Combining RCS-based size estimates and OD-based ballistic or solar radiation pressure coefficients provides rough mass estimates for unknown objects. For objects that experience measurable levels of atmospheric drag, the RCS+BC method provides mass estimates that are accurate at the 90% confidence level to within a factor of 0.47 for potential underestimations to 10.9 for potential overestimations. For objects orbiting above 450 km altitude, the RCS+SRPC method provides mass estimates accurate to within a factor of 0.44 to 5.6. These relatively large uncertainties are due in part to the fact that the mass estimation analyses use several rough approximations, such as neglecting correlations between ballistic or SRP coefficients and projected areas, as well as assuming approximate forms for the PDFs of the ballistic, SRP, drag, and reflectivity coefficients.

The analysis uses the RCS+SRPC method to estimate masses for satellites with perigee altitudes above 450 km and otherwise uses the RCS+BC method. This methodology indicates that 90% of unknown secondary objects involved in the studied CARA conjunctions have statistically expected masses between 8.1 g and 4.2 kg, with a median statistically expected mass of 0.1 kg.

Fragmentation probabilities provide the means to identify conjunctions with an elevated likelihood of creating large debris clouds. Calculated as statistical expectation values, these probabilities account for the HBR and mass estimation uncertainties inferred from the distribution of RCS and OD measurements as well as from the associated calibration processes. Using collision probabilities and fragmentation probabilities together provides the means to identify the subset of conjunctions that represent unacceptably high risks to both individual satellite missions and to the overall orbital environment. Specifically, among the CARA conjunctions analyzed in this study, fragmentation probability analysis identifies 7 to 20% of high mission risk conjunctions as also having elevated environmental risk.

## Acknowledgments

The NASA Goddard Space Flight Center funded this research through the “Flight Dynamics Support Services III” contract (contract number 80GSFC19C0072). The authors would like to thank Russell Carpenter, Steve Casali, Joseph Frisbee, Matthew Hejduk, Travis Lechtenberg, and Daniel Snow for several helpful discussions and analyses.

## References

- [1] Newman, L. K., “The NASA Robotic Conjunction Assessment Process: Overview and Operational Experiences,” *Acta Astronautica*, Vol. 66, Nos. 7–8, 2010, pp. 1253–1261.  
<https://doi.org/10.1016/j.actaastro.2009.10.005>
- [2] Tapley, B. D., Schutz, B. E., and Born, G. H., *Statistical Orbit Determination*, Elsevier Academic Press, Burlington, MA, 2004.  
<https://doi.org/10.1016/b978-012683630-1/50020-5>
- [3] Foster, J. L., and Estes, H. S., “A Parametric Analysis of Orbital Debris Collision Probability and Maneuver Rate for Space Vehicles,” NASA JSC-25898, Aug. 1992.
- [4] Akella, M. R., and Alfriend, K. T., “The Probability of Collision Between Space Objects,” *Journal of Guidance, Control, and Dynamics*, Vol. 23, No. 5, 2000, pp. 769–772.  
<https://doi.org/10.2514/2.4611>
- [5] Chan, K., *Spacecraft Collision Probability*, The AeroSpace Corp., El Segundo, CA, 2008.  
<https://doi.org/10.2514/4.989186>
- [6] Shelton, C. T., and Junkins, J. L., “Probability of Collision Between Space Objects Including Model Uncertainty,” *Acta Astronautica*, Vol. 155, Feb. 2019, pp. 462–471.  
<https://doi.org/10.1016/j.actaastro.2018.11.051>
- [7] Hall, D., “Expected Collision Rates for Tracked Satellites,” *Journal of Spacecraft and Rockets*, Vol. 58, No. 3, May–June 2021, pp. 715–728.  
<https://doi.org/10.2514/1.A34919>
- [8] Alfano, S., “Satellite Conjunction Monte Carlo Analysis,” *AAS Space-Flight Mechanics Meeting*, AAS Paper 09-233, Feb. 2009.

- [9] Schilling, B., Talib, Y., Carpenter, J. R., Balducci, M., and Williams, T. W., "Operational Experience with the Wald Sequential Probability Ratio Test for Conjunction Assessment from the Magnetospheric Multi-Scale Mission," *AAS Astrodynamics Specialist Conference*, AAS Paper 16-5424, Sept. 2016.
- [10] Hall, D. T., Casali, S. J., Johnson, L. C., Skrehart, B. B., and Baars, L. G., "High-Fidelity Collision Probabilities Estimated Using Brute Force Monte Carlo Simulations," *AAS Astrodynamics Specialist Conference*, AAS Paper 18-244, Aug. 2018.
- [11] Erwin, S., "Space Fence Radar Site Declared Operational," *Space News*, Pocket Ventures LLC of Boulder, Colorado, March 2020, <https://spacenews.com/space-fence-surveillance-radar-site-declared-operational/> retrieved 15 Dec. 2022].
- [12] Mashiku, A. K., and Hejduk, M. D., "Recommended Methods for Setting Mission Conjunction Analysis Hard Body Radii," *AAS Astrodynamics Specialist Conference*, AAS Paper 19-702, 2019.
- [13] Liou, J.-C., "Top Ten Satellite Breakups," Orbital Debris Quarterly News, NASA's Orbital Debris Program Office, July 2010.
- [14] Stokely, C. L., Foster, J. L., Stanbery, E. G., Benbrook, J. R., and Juarez, Q., "Haystack and HAX Radar Measurements of the Orbital Debris Environment," NASA, Orbital Debris Program Office Rept. JSC-62815, Nov. 2006.
- [15] Lechtenberg, T. F., and Hejduk, M. D., "Assessment and Validation of Collision "Consequence" Method of Assessing Orbital Regime Risk Posed by Potential Satellite Conjunctions," *Hypervelocity Impact Symposium*, Hypervelocity Impact Soc., Destin, FL, April 2019, HVIS2019-061.
- [16] Lechtenberg, T. L., "An Operational Algorithm for Evaluating Satellite Collision Consequence," *AAS Astrodynamics Specialist Conference*, AAS Paper 19-669, 2019.
- [17] Johnson, N. L., Krisko, P. H., Liou, J.-C., and Anz-Meador, P. D., "NASA's New Breakup Model of EVOLVE 4.0," *Advances in Space Research*, Vol. 28, No. 9, 2001, pp. 1377–1384.
- [18] Duncan, M., and Long, A., "Realistic Covariance Prediction for the Earth Science Constellation," *AIAA/AAS Astrodynamics Specialist Conference*, AAS Paper 2006-6293, Aug. 2006. <https://doi.org/10.2514/6.2006-6293>
- [19] Zaidi, W. H., and Hejduk, M. H., "Earth Observing System Covariance Realism," *AIAA/AAS Astrodynamics Specialist Conference*, AAS Paper 16-5628, Sept. 2016. <https://doi.org/10.2514/6.2016-5628>
- [20] Casali, S., Hall, D., Snow, D., Hejduk, M., Johnson, L., Skrehart, B., and Baars, L., "Effect of Cross-Correlation of Orbital Error on Probability of Collision Determination," *AAS Astrodynamics Specialist Conference*, AAS Paper 18-272, Aug. 2018.
- [21] Cerven, W. T., "Improved Empirical Covariance Estimation," *AAS/AIAA Astrodynamics Specialists Conference*, AAS Paper 13-762, Aug. 2013.
- [22] Laporte, F., "JAC Software, Solving Conjunction Assessment Issues," *2014 AMOS Technical Conference*, Maui Economic Development Board, Wailea, Maui, HI, Sept. 2014, <https://amostech.com/amos-technical-papers/>.
- [23] Papoulis, A., *Probability, Random Variables, and Stochastic Processes*, 3rd ed., McGraw-Hill, New York, 1991.
- [24] Hejduk, M. D., and Johnson, L. C., "Approaches to Evaluating Probability of Collision Uncertainty," *AAS Space Flight Mechanics Meeting*, AAS Paper 16-241, 2016.
- [25] Vallado, D. A., *Fundamentals of Astrodynamics and Applications*, 2nd ed., Microcosm Press, El Segundo CA, 2001.
- [26] Hejduk, M., Laporte, F., Moury, M., Kelso, T. S., Newman, L., and Shepperd, R., "Consideration of Collision "Consequence" in Satellite Conjunction Assessment and Risk Analysis," *International Symposium on Space Flight Dynamics*, Matsuyama, Japan, June 2017, <https://ntrs.nasa.gov/citations/20170005204>.
- [27] Baars, L., and Hall, D., "Processing Space Fence Radar Cross-Section Data to Produce Size and Mass Estimates," *AAS Astrodynamics Specialist Conference*, AAS Paper 22-586, Aug. 2022.
- [28] Arfken, G. B., Weber, H. J., and Harris, F. E., *Mathematical Methods for Physicists*, 7th ed., Academic Press, Elsevier, Waltham, MA, 2013. <https://doi.org/10.1016/c2009-0-30629-7>
- [29] Flohrer, T., Lemmens, S., Bastida Virgili, B., Krag, H., Klinkrad, H., Parrilla, E., Sanchez, N., Oliveira, J., and Pina, F., "DISCOS—Current Status and Future Developments," *6th European Conference on Space Debris*, Vol. 723, ESA Special Publication, April 2013, p. 38, <https://conference.sdo.esoc.esa.int/proceedings/sdc6/paper/163>.
- [30] Mclean, F., Lemmens, S., Funke, Q., and Braun, V., "DISCOS 3: An Improved Model for ESA's Database and Information System Characterising Objects in Space," *7th European Conference on Space Debris*, European Space Agency (ESA), Darmstadt, Germany, April 2017, Paper 151, <https://conference.sdo.esoc.esa.int/proceedings/sdc7/paper/151>.
- [31] Sivia, D. S., and Skilling, J., *Data Analysis: A Bayesian Tutorial*, 2nd ed., Oxford Univ. Press, Oxford, England, U.K., 2006.
- [32] Vouk, V., "Projected Area of Convex Bodies," *Nature*, Vol. 162, Aug. 1948, pp. 330–331. <https://doi.org/10.1038/162330a0>
- [33] Gatz, D. F., and Smith, L., "The Standard Error of a Weighted Mean Concentration—I. Bootstrapping vs Other Methods," *Atmospheric Environment*, Vol. 29, No. 11, June 1995, pp. 1185–1193.
- [34] Li, Z., Ziebart, M., Bhattarai, S., Harrison, D., and Grey, S., "Fast Solar Radiation Pressure Modelling with Ray Tracing and Multiple Reflections," *Advances in Space Research*, Vol. 61, No. 9, 2018, pp. 2352–2365.
- [35] Garcia-Pelayo, R., and Hernando-Ayuso, J., "Series for the Collision Probability in Short-Encounter Model," *Journal of Guidance Control and Dynamics*, Vol. 39, No. 8, Aug. 2016, pp. 1904–1912.
- [36] Press, W. H., Teukolsky, S. A., Vetterling, W. T., and Flannery, B. B., *Numerical Recipes in FORTRAN: The Art of Scientific Computing*, 2nd ed., Cambridge Univ. Press, New York, 1992.
- [37] Alfano, S., "Relating Position Uncertainty to Maximum Conjunction Probability," *Journal of the Astronautical Sciences*, Vol. 53, No. 2, April–June 2005, pp. 193–205.

R. Linares  
Associate Editor